

An Evaluation of CTools for H.E.S.S. Data Analysis



Daniela Guerinoni

Supervised by Professor Nukri Komin

School of Physics

University of the Witwatersrand

Johannesburg, South Africa

A dissertation submitted to the Faculty of Science, University of the
Witwatersrand, in partial fulfilment of the requirements for the
degree of Master of Science

Johannesburg, 2019

Dedicated to

Ina and Gian Guerinoni to whom I am eternally grateful

Declaration

I declare that this dissertation is my own, unaided work. It is being submitted for the Degree of Master of Science at the University of the Witwatersrand, Johannesburg. It has not been submitted before for any degree or examination at any other University.



(Signature of candidate)

03 day of November 20 20 at Alberton

An Evaluation of CTools for H.E.S.S Data Analysis

Daniela Guerinoni

Submitted for the degree of Master of Science
2019

Abstract

The present analysis of gamma-ray emissions is carried out through various detector/instrument-specific software frameworks. The structural analysis of gamma-ray sources in a H.E.S.S data set involves folding an initial source model with a spectra index-dependent point spread function to produce a model describing the expected emission of gamma-rays within the region of interest. Thus, when analysing a combination of closely separated sources, an analysis approach is needed in which the different spectral properties of each source is taken into account. The existing method for describing structural properties of gamma-ray sources within a H.E.S.S. data set involves fitting each source in the field of interest separately and ignoring any spillovers.

This project proposes an analysis technique which simultaneously fits the spectra and morphologies of multiple gamma-ray emitters with different spatial and spectral shapes. The technique involves simultaneously folding a source model for each individual source in the region of interest with the respective point spread function to produce a combined model of all the sources of interest. Such an analysis was carried out by utilising the CTools software package.

The viability of using CTools as a means of analysis of H.E.S.S. data was evaluated by determining the sensitivity of the software and how spectral and morphological results compare with that of already studied gamma-ray emitters. A simulated CTA data set served as the application domain of the former and historical H.E.S.S. data of N 157B and 30 Dor C for the latter. The results from the spectral and morphological analyses were further compared and shown in

conjunction with published findings.

It was determined that CTools is able to detect a cut-off in a CTA spectrum between 0.14 TeV and 12 TeV and can additionally distinguish confused sources, where source contamination is a factor, up to an offset of 0.05° . Ultimately, 30 Dor

C was found to have a radial disk-like morphology described by a power-law spectrum with a spectral index of -2.57 ± 0.15 and a differential flux of $(3.09 \pm 0.51) \times 10^{-19}$ ph.cm⁻².s⁻¹.MeV⁻¹. N 157B was determined to be a point source with a power-law spectrum with an associated spectral index of -2.67 ± 0.07 and a differential flux of $(1.14 \pm 0.51) \times 10^{-18}$ ph.cm⁻².s⁻¹.MeV⁻¹ within the H.E.S.S. energy range. This derived spectrum was combined with Fermi-LAT data to model the break in the non-thermal emission of N 157B.

Acknowledgements

Throughout the writing of this dissertation I have received a great deal of support and assistance. Firstly, I would like to thank my supervisor, Prof. Nukri Komin, for the guidance and patience he has shown me and whose expertise and knowledge have been invaluable in the formulation of this dissertation and throughout my masters career as a whole. I could not have imagined a better mentor for my masters study.

I would also like to acknowledge the H.E.S.S. collaboration for the use of its archival data throughout this dissertation. Additionally, this research made use of CTools, a community-developed analysis package for Imaging Air Cherenkov Telescope data. CTools is based on GammaLib, a community-developed toolbox for the high-level analysis of astronomical gamma-ray data.

I would like to thank my friends for their support throughout this process with a special feeling of gratitude directed towards the du Plessis family, in particular Sonja, Claudius and Claudius JNR, for their advice and kind motivational words and for tirelessly proof reading my dissertation. Their support and encouragement have been instrumental throughout my masters.

Finally, I would like to thank most of all my parents, Ina and Gian Guerinoni, for all the love and support, both emotionally and financially, they have shown me throughout my academic career and for all the sacrifices they have made in allowing me to pursue my masters. Throughout my personal and academic life they have given me the strength I have needed to reach for the stars and chase my dreams and their wisdom has shaped the individual I am today.

Contents

Declaration	iii
Abstract	iv
Acknowledgements	vi
1 Introduction	1
1.1 Historical Overview	1
1.2 Problem Under Investigation	3
1.3 Hypothesis	6
1.4 Aims and Objectives	6
2 Sources of Gamma Ray Emission	8
2.1 Gamma Ray Emission Mechanisms	8
2.1.1 Leptonic Process	8
2.1.2 Hadronic Process	10
2.2 Gamma Ray Sources Considered	11
2.2.1 The Crab Nebula	11
2.2.2 30 Dor C	12
2.2.3 N 157B	15
3 Ground Based Gamma-ray Astronomy	18
3.1 Production of Cherenkov Radiation	18
3.2 Imaging Atmospheric Cherenkov Telescopes (IACT)	21
3.3 Current IACT Arrays	23
3.3.1 High Energy Stereoscopic System (H.E.S.S.)	23

3.3.2	Cherenkov Telescope Array (CTA)	24
4	CTools Analysis Software	26
4.1	Overview	26
4.2	CTools and CScripts Used	28
4.2.1	<i>ctobssim</i>	28
4.2.2	<i>ctselect</i>	30
4.2.3	<i>ctskymap</i>	30
4.2.4	<i>ctlake</i>	31
4.2.5	<i>ctbutterfly</i>	32
4.2.6	<i>csresmap</i>	33
4.2.7	<i>csresspec</i>	34
4.2.8	<i>csspec</i>	34
4.2.9	<i>csiactdata</i>	35
4.2.10	<i>csfindobs</i>	35
4.2.11	<i>csiactobs</i>	36
4.2.12	<i>csmodelmerge</i>	36
5	Analysis Criteria	37
5.1	Overview	37
5.2	Log-Likelihood Values	37
5.3	P-Values	38
5.4	Significance	39
6	Sensitivity Analysis on Simulated Data	40
6.1	Analysis Pipeline	40
6.2	Cut-off Energy Sensitivity	41
6.2.1	Description of Initial Model Components	42
6.2.2	Methodology	44
6.2.3	Results	45
6.3	Disentangle Confused Sources	52
6.3.1	Description of Initial Model Components	52

6.3.2	Methodology	53
6.3.3	Results	54
6.4	Conclusion	57
7	Analysis of H.E.S.S. Data	59
7.1	Data Preparation and Reduction	60
7.2	Morphological Analysis	62
7.2.1	Morphological Models Used	62
7.2.2	Methodology	64
7.2.3	Results	66
7.2.4	Conclusion	73
7.3	Spectral Analysis	75
7.3.1	Spectral Models Used	77
7.3.2	Methodology	79
7.3.3	Results	82
7.3.4	Conclusion	88
8	Conclusions	92
	Appendix	102
A		102
A.1	Model Definition File	102
A.2	Observation Definition File	103
A.3	Abbreviations Used	105

List of Figures

3.1	Schematic Diagram Of An Electromagnetic Air Shower	20
6.2	Cut-Off Sensitivity Results For CTA Data	47
6.3	Cut-Off Energy Detection Range For CTA Data	48
6.4	Demonstration of the Deviation in the Spectral Index for Higher Cut- Off Energies	51
6.5	Disentanglement Sensitivity Results For CTA Data	55
6.6	Sky Map of Two Entangled Sources at Resolvable Offset For CTA Data	56
7.7	Sky Map of N 157B and 30 Dor C	61
7.8	XMM-Newton X-ray Flux Image	65
7.9	30 Dor C Spectrum Superimposed on the H.E.S.S. Collaboration Spectrum	70
7.10	Morphology of Test Models Superimposed on Sky Maps	72
7.11	Residual Maps of 30 Dor C	74
7.12	Non-Thermal Features of N 157B	89

List of Tables

2.1	Energy Densities and Temperatures of Photon Fields Surrounding N 157B	16
6.2	Initial Model Parameters for Cut-Off Energy Sensitivity Test	43
6.3	Initial Model Parameters for Disentanglement Test	53
7.4	Log-Likelihood Values and Event Residuals for 30 Dor C Morphology Analysis	66
7.5	P-Values and Associated Significance for 30 Dor C Morphology Analysis	67
7.6	Best Fit Parameter Values of 30 Dor C	68
7.7	Best Fit Parameter Values of N 157B	68
7.8	Non-Thermal Spectral Model Parameters	82
7.9	Log-Likelihood Values and Event Residuals for N 157B Spectral Analysis	83
7.10	P-Values and Associated Significance for N 157B Spectral Analysis	83
7.11	Best Fit Spectral Parameter Values of N 157B	84
7.12	Best Fit Spectral Parameter Values of 30 Dor C	84
7.13	Electron Population Parameters	87
A.1	General Format Of A Model Definition File	102
A.2	General Format of an Observation Definition File	104

1. Introduction

1.1 Historical Overview

The gamma ray region is a high energy region of the electromagnetic spectrum, with high energy (HE) gamma rays ranging from 100 MeV to 100 GeV and very high energy (VHE) gamma rays ranging from 100 GeV to 100 TeV. Gamma rays are produced by means of two main emission mechanisms, namely inverse Compton scattering and pion production and decay, which produce emissions over the entire gamma ray regime[1][2]. When very high energy (VHE) photons that is, gamma rays with energies greater than 100 GeV, enter the atmosphere, they interact with the nuclei of air particles to produce a cascade of ionised particles, termed air showers.

When the ionised particles of the cascade propagate with a velocity greater than that of light through the atmosphere, a pulse of blue optical light termed Cherenkov radiation is produced. The phenomenon of Cherenkov radiation was experimentally detected by P.A. Cherenkov in 1934, whereby exciting water tanks with gamma rays, Cherenkov observed a faint emission of visible radiation[3]. This phenomenon remained unexplored until Frank and Tamm performed theoretical studies of the emission mechanism of Cherenkov radiation in 1937 and went on to formulate a theory inclusive of the particulars and characteristics on the subject[3][4].

The theory of Cherenkov radiation was extended to gases by Blackett in 1948, in particular the event of gamma ray photons propagating through the atmospheric medium[5]. Blackett theorised that the Cherenkov radiation as a result of air showers accounts for approximately a ten-thousandth of the light intensity of the night sky.

He pointed out that such a light pulse with a substantially low intensity prompts for new detection methods[5].

Galbraith and Jelley[6] proposed that placing a photomultiplier at the focus of a large optical reflector connected to an oscilloscope may be able to amplify the low intensity of Cherenkov radiation and allow for a successful detection of Cherenkov radiation[5]. In 1952 they succeeded in detecting light pulses which corresponded to the theorised characteristics of Cherenkov radiation, marking the first successful detection of Cherenkov radiation produced by air showers. This detection brought with it the possibility to study gamma rays by means of Cherenkov light.

The era of gamma-ray astronomy made headway in 1958 when P. Morrison[7] put forward evidence to suggest VHE gamma ray emissions from the Crab Nebula with detections possible at 100MeV[1]. A year later in 1959 G. Cocconi[8] proposed that the arrival direction of TeV photons may be determined by studying the arrival front of air showers generated when the incoming photons interact with the atmosphere. The idea of studying gamma rays by analysing the Cherenkov radiation using imaging techniques gained momentum in the subsequent years and the implementation of Imaging Atmospheric Cherenkov Telescopes (IACTs) was prompted. IACTs were pioneered by the Whipple observatory in Arizona USA. In 1989, Whipple made the first firm detection of gamma rays from the Crab Nebula[9], which marked the point at which TeV astronomy became prominent.

Over the past decade, the current generation of IACTs (H.E.S.S, CTA, MAGIC and VERITAS), which are based on the Whipple design, have proceeded to detect and confirm several gamma-ray sources, ranging from 100 GeV to 100 TeV[1]. Some of the detected sources include blazars, such as the large elliptical galaxy Markarian 421 in 1992[10] as well as gamma ray emissions from radio galaxies like M 87[11][12], a giant elliptical galaxy located in the central region of the Virgo cluster of galaxies. Supernova remnants like N 132D[13] as well as pulsar wind nebulae like N 157B[13] have also been detected, by means of imaging atmospheric Cherenkov techniques,

to emit in the TeV regime.

1.2 Problem Under Investigation

The analysis of gamma ray emissions is currently dependent on a variety of software frameworks that are specific to each detection instrument. The structure of gamma ray sources in a H.E.S.S data set is analysed by means of the following procedure.

The dependence of the radiative flux density of a gamma ray source on the energy is determined by means of simulations for a given spectral index, typically one associated with the gamma ray emitter under consideration. Thereafter, the point spread function (PSF) which best describes this dependence is generated.

The PSF is the probability distribution of reconstructed event positions of a source. It describes the angular distribution of photons based on the reconstruction of the shower direction and the photon energy. The PSF is averaged over the entire data set and later used for the fitting of both source position and source morphology.

The spectrum of the gamma ray emitter may be studied by initially considering the energy distributions of events within the region of interest, which is determined by means of aperture photometry. The process of aperture photometry entails measuring the brightness of a source by summing the counts within a particular aperture which is centred on the source. The light from the area surrounding the source is also collected within this aperture and is corrected for by means of determining the counts within an annulus surrounding the aperture. Once the energy distribution of events is determined, an initial spectral model, such as a power law or log-parabola, is fitted.

The morphology of the gamma ray source of interest is determined using the surface brightness of the emitter in conjunction with an initial assumption of the

position angle, central coordinates and the semi-major axis. The degree by which the source deviates from circularity is also taken into account. These parameters are iteratively fitted to the observed data until the residuals produced are sufficiently small; that is, until the fit produces a predetermined significance threshold.

The previously described morphological analysis approach, while being quite powerful, is not without certain limitations. Since the PSF was generated for a specific spectral shape, the source model folded with the PSF is only valid for one source within the region of interest. If multiple sources are required to be fitted, certain assumptions must be made. The sources under consideration must be sufficiently separated, by an angular separation of at least 1° , and a separate analysis must be performed; meaning that each source is fitted separately. For multiple sources with an angular separation of less than 1° , the sources must be fitted simultaneously; that is, a PSF is generated for an average spectrum of the sources under consideration and the sources are fit together. This approach is valid under the assumption that the sources have similar spectral shapes.

This technique was implemented by the High Energy Stereoscopic System (H.E.S.S) Collaboration et al.[13] for three sources within the Large Magellanic Cloud (LMC) with an angular separation of 0.1° . The LMC was observed with H.E.S.S for a total of 210 hours of deep exposure in the VHE gamma ray regime. Three sources were detected and studied, namely the pulsar wind nebula of the pulsar N 157B, the radio loud supernova remnant N 132D and the non-thermal X-ray shell 30 Dor C.

Thus, the only method to fit the morphology of multiple sources with different spectra within a H.E.S.S. data set is to fit each source separately and ignore spillovers from neighbouring sources. This project proposes a solution to this by simultaneously fitting the spectra and morphologies of multiple gamma-ray emitters with different spectral and spatial shapes by utilising the CTools software and applying it to a H.E.S.S. data set.

Morphological analysis performed by CTools is carried out by folding an initial source model which describes the spatial extent of the emitter with the PSF. This results in a model which describes the expected emission of gamma rays within the region of interest. The initial model may assume various spatial forms, such as point-like or even gaussian-like. Thereafter, the folded model is fitted to observational data. An analysis technique of a similar nature has been successfully implemented in Fermi-LAT data analysis[14].

CTools is a software package that is specifically designed for the analysis of Cherenkov Telescope Array (CTA) data as well as existing data from other IACTs such as MAGIC, H.E.S.S. and VERITAS, provided that the data format follows that of CTA. The CTools software package allows for a variety of applications, such as a maximum likelihood model fit, as well as the creation of spectra, light curves and images of gamma-ray emitters, and makes use of reconstructed IACT events. IACT instrument response functions are required in order to describe the transformation of physical photon properties to the properties of measured events. The only external library dependency of CTools is Gammalib, which is widely used in Fermi-LAT analysis[15]. CTools version 1.5.2 will be used throughout this paper.

Studies using CTools to analyse IACT data have been performed which have already produced successful outcomes. For example, Mohrmann et al[16] used CTools analysis methods to perform a 3D likelihood analysis of public data provided by the H.E.S.S. Collaboration and produced results which coincide with that produced using standard analysis techniques as well as published H.E.S.S. results.

Knödseder et al[17] have had very recent success in analysing publicly available H.E.S.S. data of the Crab Nebula, MSH 15–52, RX J1713.7–3946, and PKS 2155–304 with CTools. They produced a background model which was able to describe the background rates of the H.E.S.S. data based on the reconstructed energy and event direction for each observation. Using this model in conjunction with other CTools analysis methods, they were able to analyse the previously mentioned sources and

produced results which were in agreement with that produced by H.E.S.S. using other analysis methods.

1.3 Hypothesis

This project hypothesises that by adopting an analysis technique, as implemented by CTools, which folds a source model for an individual source with the PSF, which is generated based on the spectral index associated with that individual source, a combined model consisting of all the folded models for all sources within the region of interest may be produced. Fitting the combined model to H.E.S.S data will allow for an improvement in the resolution of H.E.S.S data and allow one to gain insight on the form of gamma-ray emitters and better distinguish sources with an angular separation of less than one degree while simultaneously determining their spectral shape.

1.4 Aims and Objectives

This project aims to evaluate the CTools analysis framework on simulated CTA data and apply the framework to existing H.E.S.S data of the Large Magellanic Cloud (LMC) in an attempt to increase the resolution of H.E.S.S. data analysis.

The evaluation criteria will consist of the ability of the software to resolve two closely separated CTA sources, where source contamination is a factor, as well as the sensitivity of the software to detect a deviation in the spectral energy distribution of a CTA source, namely a cut-off energy. The application domain of the software includes fitting the spatial and spectral shapes of gamma-ray emitters for a H.E.S.S. data set of the LMC. This, in turn, may aid in understanding and conceptualising the form of gamma ray sources and will help to better differentiate gamma-ray emitters with small angular separations and identify deviations in the spectral energy distribution of gamma-ray emitter.

The objectives of this project include initially evaluating the sensitivity of CTools to detect a cut-off energy of a single gamma ray emitter, that being the Crab Nebula, for a simulated CTA data set. This process includes performing iterative maximum likelihood fitting, both morphological and spectral components, of various source models to a series of simulated CTA data.

Thereafter, the degree of resolution of the CTools software will be explored by analysing two closely separated gamma ray emitting sources, the Crab Nebula and a pseudo source. Again, the sources will be fitted to simulated CTA events, which, as before, involves maximum likelihood fitting of all source model components to the simulated CTA data.

Further objectives include applying the CTools software to real data, i.e. H.E.S.S. data, by fitting the morphology and spectrum of gamma-ray emitters in the LMC, namely N 157B and 30 Dor C, and fitting multiple sources with various spectral shapes and morphologies simultaneously to existing data and assessing the validity of the results.

The success or failure of the application of CTools to H.E.S.S data will be determined by considering the maximum log-likelihood value after fitting the respective models to the corresponding data set as well as inspecting the best-fit parameters and spatial and spectral residuals. Other statistics including p-values and significance will also be considered. The results of the fits regarding N 157B and 30 Dor C will be compared with existing data provided by the H.E.S.S. collaboration in the gamma ray and other energy regimes of the electromagnetic spectrum in order to ensure the validity of the results.

A pedagogical approach will be taken in studying the general analysis framework of CTools and its various applications and executables as well as becoming familiar with H.E.S.S data analysis and gamma ray emitting sources.

2. Sources of Gamma Ray Emission

The present chapter discusses the various mechanisms by which gamma ray photons are emitted, both in a leptonic and a hadronic sense. A description of both morphological and spectral properties of the sources considered within this paper, namely the Crab Nebula, 30 Dor C and N 157B is also present. The information regarding N 157B and 30 Dor C is provided by the H.E.S.S. collaboration, obtained by performing a deep exposure of 210 hours of the 30 Doradus nebula, and serves as a basis to which the results produced using CTools may be compared.

2.1 Gamma Ray Emission Mechanisms

Gamma ray photons are generally produced by two main emission mechanisms which may be categorised as either leptonic or hadronic processes. The possibility exists for both process to contribute to the overall spectral energy distribution of a gamma ray source.

2.1.1 Leptonic Process

The leptonic scenario involves high-energy electrons interacting with low-energy photons by means of the processes of inverse Compton scattering. Electrons which traverse a magnetic field will experience a change in trajectory as a result of the magnetic field. That is, an electron will experience an acceleration perpendicular

to its velocity, causing it to spiral along the magnetic field. This change of trajectory will prompt the release of synchrotron radiation, generally from the radio to the x-ray regime[3]. Thereafter, the same population of ultra-relativistic electrons allow for the upscattering of the previously produced synchrotron photons or other nearby photon fields to higher photon energies, of the gamma ray domain, in inverse Compton processes[3].

It follows that the spectral energy distribution of typical gamma ray emitters, such as pulsars, pulsar wind nebulae (PWN) and supernova remnants (SNR), will consist of a synchrotron region as well as inverse Compton emission[18].

The synchrotron region is dominant at lower energies up to X-ray energies, and is most prominent in stronger magnetic fields. For example, in the case of PWN and SNR the synchrotron region will be most prominent in early evolutionary stages, that being when the associated magnetic field is stronger and hasn't begun to weaken as a result of the expansion of the emitter[19].

Typically, the synchrotron region is described by a power law with a characteristic peak[18]. This high energy peak represents the cooling of the electrons which promote the release of synchrotron radiation and is known as the electron cooling break. Higher energy electrons will experience an energy loss at a faster rate than that of lower energy electrons[18][19]. Therefore, the spectral energy distribution will experience a steepening at a particular electron energy. This is the energy at which the break occurs and is identified as the energy at which the age of the gamma-ray emitter is equal to the cooling time of the higher energy electrons. The electron cooling time is related to the magnetic field strength of the gamma-ray emitter, that is, a stronger magnetic field will result in a smaller electron cooling time. Therefore, the energy at which this cooling break occurs may impart information regarding the age of the gamma ray emitter[18].

The inverse Compton region is dominant at higher (gamma-ray) energies, and is

more prominent in older gamma ray emitters as the emitter accumulates more particles in its vicinity, which may serve as up-scattering surfaces for the synchrotron photons[19]. Often radiation fields, such as cosmic microwave background radiation and companion stars, may serve as additional up-scattering surfaces for the synchrotron photons which in turn would increase the dominance of the inverse Compton region of the gamma ray emitter itself. As per the synchrotron region, the inverse Compton region is usually described by a peaked power law, with the peak resulting from particle cooling.

The characteristic shape of both the synchrotron region and the inverse Compton region may be modified by other processes, such as self-absorption as well as strong and weak magnetic fields associated with the emitter itself, but generally follow a power law.

2.1.2 Hadronic Process

The hadronic process involves collisions between relativistic protons and dense areas of the interstellar medium. When these relativistic protons scatter off nuclei of interstellar gas, mesons are produced, namely π^0 , π^+ and π^- . In particular, the neutral meson, π^0 , has an energy of 135 MeV and upon decaying releases two gamma rays whose spectrum reaches a maximum differential flux of approximately half that of the neutral pion energy, that is approximately 68 MeV. The spectrum of these gamma rays decreases from the maximum according to a power law relation[3].

The dominance of the gamma ray emission process depends entirely on the type of emitter. Scenarios exist where hadronic processes are prevalent, as is the case of the supernova remnant RX J1713.7-3946. Berezhko et al.[20] discerned that explaining the gamma ray emissions by means of purely leptonic processes would require a magnetic field with an unrealistically uniform strength. It was concluded that the observed synchrotron spectrum of the supernova remnant is not in agreement with a purely leptonic scenario, which strongly supports the case of hadronic dominated

emission.

Conversely, the gamma ray emission produced by the Crab Nebula is best described by a leptonic scenario in which the gamma ray luminosity is dependent on the intensity of the surrounding photon fields by means of inverse Compton scattering [13]. It is also possible that observed properties of an emitter are better explained by considering a combination of these emission processes.

2.2 Gamma Ray Sources Considered

The three gamma ray emitters considered in this paper include the Crab Nebula, the superbubble 30 Dor C and the pulsar wind nebula N 157B. In the present section, a brief description of both morphological and spectral properties of the three sources are given. Note that only simulated data of the Crab Nebula is studied in this paper with modified spectral and morphological properties necessary for the purpose of the study. Since the Crab Nebula is not actually being analysed but rather being used as a tool to assess software, the particulars of the Crab Nebula, such as spectral and spatial distributions, may not entirely coincide with those of chapter 7.

2.2.1 The Crab Nebula

The Crab nebula is a supernova remnant (SNR), a by-product of the Crab pulsar, PSR B0531+21, with an energy loss rate of 4.6×10^{38} ergs.s⁻¹, located within the Milky Way galaxy, with a right ascension and declination of 83.5° and 22°, respectively. To date, the Crab Nebula is one of the most powerful gamma ray emitters within the Milky Way[13].

The Crab nebula has been observed over a variety of photon energy regimes, including radio, optical, x-ray and gamma ray energies. The spectral energy distribution of the Crab Nebula exhibits a synchrotron peak in the radio and the x-ray regime, with a secondary peak, as a result of inverse Compton scattering, dominat-

ing the gamma ray regime. The presence of a combination of both a synchrotron and inverse Compton peak is the result of high-energy electrons interacting with the magnetic field of the nebula to release low energy-photons. These low-energy photons later interact with the same population of electrons to emit in the TeV regime in a process known as synchrotron-self-Compton. Cosmic microwave background (CMB) photons also make a contribution to the observed gamma ray emissions[1][21].

A study carried out by Aharonian et al[21] measured the energy spectrum of the Crab Nebula with the HEGRA IACT system. The observation was conducted over two separate sessions from September 1997 to March 1998 and from October 1998 to April 1999. It was found that the Crab Nebula energy spectrum is consistent with a pure power law in the energy range of 1TeV to 20TeV with a differential flux measuring $2.79 \times 10^{-17} \text{ ph.cm}^{-2}.\text{s}^{-1}.\text{MeV}^{-1}$ and a spectral index of -2.59. However, Aharonian et al[22] conducted further observations of the Crab Nebula in 2006 using H.E.S.S. and found that an exponentially cut-off power law was a more appropriate description of the Crab spectrum. It was concluded that the observed Crab spectrum experiences a cut-off at 14.3 TeV with a differential flux of $3.7 \times 10^{-17} \text{ ph.cm}^{-2}.\text{s}^{-1}.\text{MeV}^{-1}$ and a -2.4 spectral index.

2.2.2 30 Dor C

The 30 Doradus Nebula, otherwise known as the Tarantula Nebula, is a large star-forming region found within the Large Magellanic Cloud (LMC), a neighbouring galaxy to the Milky Way[23]. The 30 Doradus Nebula emits across the electromagnetic spectrum, making it a subject of interest for multi-wavelength studies including optical and infra-red observations as well as gamma-ray and X-ray surveys[24].

For the purpose of this paper, the gamma ray regime of the 30 Doradus Nebula will be the area of interest, with particular focus given to the superbubble 30 Doradus C, abbreviated to 30 Dor C.

When a massive star reaches the end of its evolution and experiences a core collapse via a supernova explosion, large amounts of high energy ejecta are propagated outward at very high speeds over a substantially short time scale, "shocking" the surrounding interstellar medium[25]. Additionally, massive stars produce powerful and energetic stellar winds which sweep up surrounding the interstellar medium[25]. Star clusters containing tens of these massive stars will experience several supernovae explosions in conjunction with a multitude of stellar winds. As a combination of these occurrences propagate within the cluster, the surrounding interstellar gas will be swept up by a high temperature shock wave and will accumulate into a shell of dense, shocked gas, leaving a large hot cavity in its wake. This process results in a super-bubble, within the interstellar medium[26][27].

In particular cases the shock waves produced from the explosions and winds accelerates the interstellar gas substantially, including specifically the constituent electrons, such that energies above 1 TeV are attained. As a result, a shell emitting non-thermal x-rays is produced by means of the synchrotron emission process[28], as is the case of 30 Dor C. Non-thermal x-ray emissions were initially detected by the Einstein observatory[29] within the vicinity of the 30 Doradus nebula in 1981. In 2001 where Dennerl et al[30] produced the first x-ray images and spectra of sources within the 30 Doradus region, including 30 Dor C.

In conjunction with the non-thermal x-rays, 30 Dor C also emits TeV gamma rays. Superbubble VHE gamma-ray emission from 30 Dor C was detected by the H.E.S.S. collaboration[13] in a 210 hour observation of the LMC. These gamma ray emissions may be attributed to the inverse Compton scattering mechanism whereby electrons, of the same population as those causing the non-thermal x-ray emission, impart energy to low-energy photons, elevating them to gamma ray energies[13].

The fact that 30 Dor C emits both gamma rays and X-rays suggests a fast expanding shell in order for the shell electrons to be accelerated to X-ray synchrotron-emitting energies. Thus, large shock wave velocities are required. According to

a study carried out by the H.E.S.S. collaboration[13] on TeV gamma ray emitters within the LMC, this shock wave velocity is approximately 3000 km.s^{-1} .

In addition to the observed gamma ray and x-ray emissions from the 30 Dor C superbubble, both radio as well as optical radiation is also observed from the shell. Radio emissions from 30 Dor C were initially identified by Le Marne[31] in 1968. A shell-like structure, characteristic of a superbubble, was identified by Mills et al[32] in 1984 with an angular diameter of $5.9'$, equivalent to a radius of approximately 40 pc. Later in 1985, Mathewson et al[33] used the Anglo-Australian telescope to perform further observations of 30 Dor C. By using narrow band interference filters, optical images of large filamentary structures coincident with radio observations of 30 Dor C were produced.

These emissions result from both stellar winds and supernovae within the OB association named NGC 2044[13]. NGC 2044 is not the only close companion of 30 Dor C. Present on the outskirts of the superbubble is the young supernova SN 1987A as well as the pulsar wind nebula N 157B and present within the super bubble is the star cluster of the LH 90 association[13].

Spectral studies in the gamma-ray regime revealed 30 Dor C to follow a power law spectrum with a spectral index of -2.6 ± 0.2 and a differential flux of $(1.6 \pm 0.4) \times 10^{-19} \text{ cm}^{-2} \cdot \text{s}^{-1} \cdot \text{MeV}^{-1}$ [13]. The flux for 30 Dor C was determined by means of reconstructing the flux within a 0.07° centred on 30 Dor C; however, a portion of gamma rays emitted from N 157B falls within this region, resulting in a flux contamination of approximately 29% and, therefore, a larger reconstructed flux for 30 Dor C. Thus, the H.E.S.S. collaboration were required to compensate for this. It follows that the flux previously presented is the flux after correction for the contamination has been applied. Further studies performed by the H.E.S.S. collaboration using observations obtained from XMM-Newton in the 0.5 keV to 8 keV x-ray energy band reveal 30 Dor C to be at a mere 0.15° offset from N 157B with a right ascension and declination of $83.98^\circ \pm 0.02^\circ$ and $-69.18^\circ \pm 0.01^\circ$ respectively.

2.2.3 N 157B

In particular circumstances when a star reaches the end of its evolution and experiences a gravitational collapse, a rapidly rotating neutron star, which is incredibly dense and highly magnetic, is produced. As time progresses the spin period of these stars increases, indicating a loss of rotational kinetic energy, termed spin-down energy loss. This energy loss is then imparted on surrounding electrons and positrons which accumulate to form a nebula of ultra-relativistic particles, termed a Pulsar Wind Nebula(PWN)[13][19].

Generally, PWNe which are still early in their evolution are completely enveloped by the SNR of the parent pulsar and are presented as point-like sources, which may be resolvable by IACTs[1]. As PWNe progress through their evolution, they tend to undergo an expansion. Additionally, it is possible to describe the spatial extent of the emission within the TeV regime[1].

The PWN N 157B, powered by the powerful pulsar PSR J0537-6910 located within the LMC, is the final gamma ray emitter considered in this paper. As mentioned before, N 157B is a close neighbour of 30 Dor C, offset by 0.15° [13] with a right ascension of $84.43^\circ \pm 0.003^\circ$ and a declination of $-69.17^\circ \pm 0.003^\circ$ [18]. Both non-thermal x-ray and gamma ray emissions as well as radio emission have been detected from N 157B. The x-ray and radio signal of N 157B is attributed to synchrotron emission as a result of the ultra-relativistic particles propagating through the strong magnetic field of the pulsar itself. By means of inverse Compton scattering of surrounding infrared photon fields and the CMB, high-energy gamma rays are emitted[13][34].

The H.E.S.S. collaboration[18] conducted a study in which the gamma-ray spectrum in conjunction with radio and X-ray emissions was described by a multi-zone leptonic model with the inverse Compton and synchrotron emission originating from

a single relativistic electron population. It was concluded that N 157B has a high spin-down energy loss rate of $4.9 \times 10^{38} \text{ erg.s}^{-1}$, similar to that of the Crab pulsar. The star cluster LH 99, consisting of hot, blue giant stars and both warm and cold dust, lies close to N 157B, either in front or surrounding the nebula[13] and has strong associated infrared photon fields. These infrared photon fields in conjunction with cosmic microwave background radiation and the 30 Doradus nebula[13] act as scattering surfaces for synchrotron photons and, thus, contribute to the inverse Compton emission of high-energy gamma rays as well as some radio and X-ray emissions. This in conjunction with the high spin-down power, makes N 157B an extremely bright gamma ray emitter[18]. The energy densities and temperatures of these photon fields are presented in table 2.1.

Table 2.1: Energy Densities and Temperatures of Photon Fields Surrounding N 157B. The table values have been adapted from the H.E.S.S. collaboration et al[13]

Photon Field	Temperature (K)	Energy Density (eV.cm^{-3})
CMB	2.7	0.26
30 Dor C	88	2.7
LH 99 (Cold Dust)	29	12.7
LH 99 (Warm Dust)	230	5.7

The relativistic electron population, which upscatters the surrounding photon fields, follows a broken power law in the energy range 1 eV to 10^{15} eV. The H.E.S.S. collaboration assumed two breaks in the electron spectrum, one lower energy, intrinsic break of 54 GeV and a high-energy cooling break at 1.1 TeV, representing the cooling break in the inverse Compton regime[18].

More concretely, the H.E.S.S. collaboration[18] put forth a model which assumes that the cooling break occurs at an energy at which the synchrotron loss time is equivalent to the age of the PWN. With this assumption in place, the model predicts that the total energy stored in the relativistic electron population is $4 \times 10^{49} \text{ erg}$. Furthermore, a spectral index of -2.60 was predicted for X-ray to TeV data and a

cut-off of 1.1 TeV was anticipated[18] for the multi-zone model.

In another study performed by the H.E.S.S. collaboration[13], only the gamma ray regime of N 157B was considered. The study found that assuming a point-like source morphology, when considering gamma ray emission, results in the best fit position since the diameter of N 157B is of the order of the angular resolution of H.E.S.S. data[13]. However, N 157B does exhibit a comet-like morphology overlaid on diffuse emission in the x-ray regime, indicating no exact correlation in morphologies across the various emitted energy regimes.[35]. A power law best describes the spectrum of N 157B from 1 TeV to 12 TeV, with possible deviation at higher energies, with a spectral index of 2.8 ± 0.1 and a differential photon flux of $(1.3 \pm 0.1) \times 10^{-18} \text{cm}^{-2} \cdot \text{s}^{-1} \cdot \text{MeV}^{-1}$ [13].

3. Ground Based Gamma-ray Astronomy

This chapter offers a description of the production of Cherenkov radiation and how it serves as a means of detection and analysis of gamma ray emitters. Also included is a brief description of the general principle of operation of IACTs as well as a discussion of the IACTs from which data sets for this paper were used, namely H.E.S.S. and CTA.

3.1 Production of Cherenkov Radiation

In general, the Earth's atmosphere is transparent to radiation with energies up to the order of 10^2 eV. Higher energy radiation, however, is unable to penetrate the atmosphere as a result of interactions with air molecules. Thus, upon entering the Earth's atmosphere, high energy photons, of energy 10^6 eV to 10^{12} eV, from gamma ray sources will undergo an interaction with atmospheric particles.

When a high energy photon passes in the vicinity of an atmospheric nucleus, the electric field of the nucleus causes the photon to transform into an electron and positron pair by means of pair production. As suggested by Heitler[36] in 1984, the photon energy is shared equally between the pair; thus, the energy of the initial gamma ray photon must be at least twice that of the rest mass energy of an electron. Excess photon energy is converted into kinetic energy of the electron-positron pair.

As these electrons and positrons propagate through the atmosphere, they are decelerated by other atmospheric nuclei and release secondary gamma rays through the Bremsstrahlung process. This cycle is repeated such that a cascade of electrons, positrons and secondary gamma rays is produced, forming an electromagnetic shower of particles directed towards the Earth's surface[37]. This phenomenon is graphically displayed in Figure 3.1. Note that electromagnetic air showers are not to be confused with hadronic air showers which are observed at much greater widths as a result of the high transverse momentum associated with pions produced in the cascade.

The cascade will continue to propagate until the point at which the energy of the individual photons and electron-positron pairs are too low for pair-production or bremsstrahlung to take place. At this point the penetration depth of the electromagnetic shower is reached[36].

Additionally, the charged particles, that is the electrons and positrons, polarize the atmospheric molecules while propagating through the atmosphere, creating a dipole field in the vicinity of the trajectory of the charged particles. When the charged particles are no longer in the vicinity of the atmospheric molecules, the molecules revert back to their ground state and in turn emit electromagnetic radiation[38]. Cherenkov noted and studied this phenomenon in 1936 and concluded that he had discovered a new mechanism for radiation production.

Since gamma ray photons impart all of their energy upon decaying into electron-positron pairs, these charged particles are highly energetic and propagate through the atmosphere with a velocity v that exceeds the phase velocity of electromagnetic radiation in the atmospheric medium[38]. As a result, a coherent wave front, travelling with a velocity v , is generated from the accumulation of wave fronts of the previously emitted electromagnetic radiation. This wave front appears as a blue cone-like flash of light, termed Cherenkov radiation. Frank and Tamm[39] came to this conclusion in 1937 upon performing theoretical studies of Cherenkov's work.

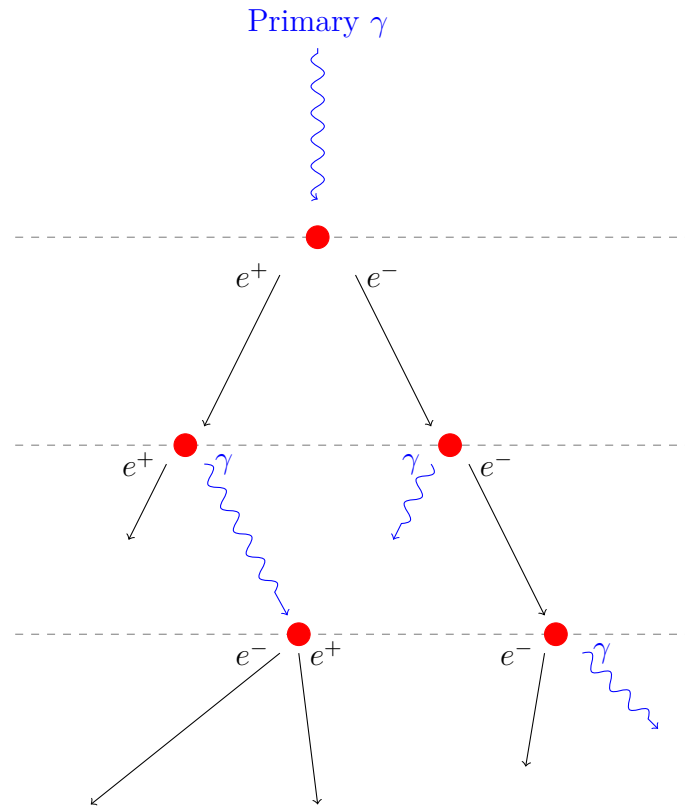


Figure 3.1: Schematic diagram of an electromagnetic air shower. The above figure demonstrates a primary gamma ray interacting with an atmospheric molecule to produce a cascade of secondary particles. Atmospheric molecules are represented by red dots while gamma rays by blue lines and electrons and positrons by solid black lines.

They theorised that when the ratio between the wave front velocity and the speed of light in the atmospheric medium, termed β , is greater than the reciprocal of the refractive index, n , of the medium under consideration, that is to say

$$\beta > \frac{1}{n},$$

where $\beta = \frac{v}{c}$

Cherenkov photons are emitted in a cone-like shape at an angle θ to the original direction of the charged particle which caused the emission of the photon, where θ is defined according to:

$$\cos \theta = \frac{1}{\beta n},$$

In the case that the air shower propagates along the axis of the primary gamma ray photon, with little lateral spreading of charged particles and gamma ray photons, Cherenkov light will be emitted at the characteristic Cherenkov angle when the cascade reaches the threshold of its development. At higher altitudes where the atmospheric density is much lower, the emission angle θ will be much less as a result of fewer interactions with atmospheric particles. The converse is true for lower altitudes where the atmospheric density is much greater. The emission angle will increase as a result of an increase in the number of interactions with atmospheric particles[40].

Thus, the angle of the wave front is dependent on the refractive index of the atmospheric medium. Frank and Tamm's theory was later tested by Cherenkov in 1937, where he was able to demonstrate the relationship between the angle of photon emission and the phase velocity of the charged particle, as predicted by Frank and Tamm[39].

Cherenkov light emitted from the electromagnetic cascade may be used to form a low resolution image of the shower from which the length and width of the shower may be determined and the arrival direction of the primary gamma rays may be estimated[40].

3.2 Imaging Atmospheric Cherenkov Telescopes (IACT)

As discussed in the previous section, high energy gamma rays are unable to penetrate the Earth's atmosphere and will, therefore, interact with atmospheric particles to produce electromagnetic air showers, resulting in Cherenkov radiation. The Cherenkov radiation is beamed in a cone-like shape on the Earth's surface around

the area of the incident charged particle.

The aforementioned gamma rays may be detected by means of either ground-based methods or space-based methods. Due to the low fluxes associated with high-energy photons in the TeV regime, a larger collection area is needed, making space based detection for this energy regime not viable. Thus, ground based methods must be implemented.

Since these high energy gamma rays are unable to penetrate the Earth's atmosphere, direct detection methods at ground level are not possible. Thus, gamma-ray astronomy in the TeV regime uses the phenomenon of Cherenkov radiation in order to perform observations. Jelly et al[6] proposed that this Cherenkov radiation may be detectable by optical means, pioneering the way for the development of Imaging Atmospheric Cherenkov Telescopes (IACTs)[41].

Generally, IACTs comprise of a large optical reflector used to direct the incoming Cherenkov photons on an array consisting of several hundred photomultipliers mounted in the focal plane of the reflector[1]. The width of the associated PSF is usually approximately 0.05° [1]. If an IACT falls within the area of Cherenkov light, the photomultipliers receive the Cherenkov photons which are absorbed by an electron contained within the photomultiplier. The electron is released, by means of the photoelectric effect, and is accelerated through the high voltage field of a chain of dynodes. The dynodes serve to amplify the electron signal through secondary emissions such that the received photons have a measurable effect. Ultimately the photomultiplier converts the radiation into an electrical signal that can be measured and recorded. This electrical signal is then reconstructed into an image showing the trajectory of the **air shower**, **making** it possible to discern the direction to celestial objects from which the primary gamma ray originates. Flux and intensity measurements are also possible[41].

IACTs are well suited for the detection and study of gamma ray sources since the

number of shower particles is proportional to the radiated Cherenkov light, making estimations of the energy of the gamma ray source possible. Additionally, the photomultipliers are capable of capturing the fast Cherenkov light flash and handling the fast rate of incoming data[41].

It is rather challenging to reconstruct the geometry of the gamma ray shower with a high degree of accuracy when a single reflector is used, motivating the use of stereoscopic array of reflectors in order to reconstruct the true gamma ray shower geometry.

3.3 Current IACT Arrays

H.E.S.S. and CTA form part of the third and fourth generation of IACTs respectively. Both utilise several IACTs which observe the particle showers at various points, allowing for a more refined reconstruction of the geometry of the air shower.

3.3.1 High Energy Stereoscopic System (H.E.S.S.)

The High Energy Stereoscopic System (H.E.S.S.), situated in Khomas, Namibia, was developed with the purpose of performing observations of the southern sky. In 2003, the design criteria and component specifications of H.E.S.S. as a whole were described[42]. H.E.S.S. consists of five optical reflectors in total: four 12 m mirrors arranged in a square with a side length of 120 m and a central 28 m mirror. The telescope array is focused at a height of 10 km, approximately the height at which Cherenkov radiation is emitted. The spacing allows for at least two reflectors to fall within a Cherenkov light pool, which is, on average, 250 m wide[42][43][44].

The four 12m optical reflectors consist of 380 mirror segments which follow the Davies-Cotton layout[42], producing approximately 100 m² of mirror area per reflector. That is, each circular mirror segment shares the same focal length which

is identical to the overall focal length of the reflector. The segments are arranged on a spherical surface with a radius equal to that of the focal length[42]. Each of the four reflectors has a camera, mounted at the focal length of the reflector, connected to an array of photomultiplier tubes. Each camera has a 5° field of view, making it possible for the reflectors to study extended gamma ray sources. The cameras consist of 960 pixels with a size of 0.16° . The mirror segments are capable of focusing approximately 80% of the radiation received within a 0.03° radius[42].

Unlike the 12 m reflectors, the central 28 m reflector follows a parabolic layout where 875 hexagonal mirrors are arranged on a parabolic surface with varying focal lengths[42]. The camera setup for the 28m reflector follows that of the 12m reflectors; however, the field of view, 3.2° , and the pixel size, 0.067° , are considerably less. The 28m reflector contributes 600m^2 of collection area to the overall array. The smaller pixel size and the decreased field of view improves the overall angular resolution of the telescope array to less than 0.1° . All five reflectors produce an energy resolution of approximately 15% which allows for H.E.S.S. to probe gamma ray sources in the energy range of 50 GeV to 100 TeV[43]. Before the addition of the 5th larger telescope, the energy range was narrower at 700 GeV to 100 TeV.

The sensitivity of H.E.S.S. in the aforementioned energy range allows for flux measurements up to a few thousandths of that of the Crab Nebula[43][44]. This high sensitivity has made the detection of faint VHE gamma-ray sources, such as NGC 253 a galaxy with a flux approximately 0.3% of the Crab Nebula, possible[43].

The effective area of H.E.S.S. increases with the energy range under observation. More specifically, the effective area ranges from 10 m^2 to approximately 10^6 m^2 in the range of 100 GeV to 10 TeV[45].

3.3.2 Cherenkov Telescope Array (CTA)

The design and layout of the Cherenkov Telescope Array (CTA) deviates from that of H.E.S.S. The southern CTA array, located in Chile, covers a 4km^2 area consisting

of a total of 99 reflectors spaced at approximately 100m from one another. The increase in the array area allows for the collection of more events and, thus, is capable of probing gamma ray sources between 20GeV and 300TeV, greater than that of H.E.S.S. The reflectors which constitute the telescope array vary in size. Four 23m large reflectors, twenty five 12m medium reflectors and seventy 4m small reflectors form part of the array[44].

The large reflectors follow a parabolic layout while the medium reflectors favour the Davies-Cotton design. The small reflectors vary between the Davies-Cotton layout and the Schwarzschild-Couder where two different mirror segments are used. The cameras of the large reflectors have a field of view of 4.3° and pixel size of 0.09° while the medium reflector allows for 8° field of view with a 0.18° pixel size[43]. The variety of the small reflectors allows for a field of view ranging from 8° to 10° with a 0.25° pixel size[43].

The differences in CTA compared to H.E.S.S. offer an overall increase in the angular resolution of gamma ray sources, from 0.1° to approximately 0.01° . The design also offers an overall increase in the energy resolution, to approximately 10%, compared to H.E.S.S. for the aforementioned energy range[44][46]. When considering sensitivity, CTA aims for an overall improvement of one magnitude over H.E.S.S. and other current IACT instruments at 1 TeV energies[43]. The effective area of CTA follows a similar trend to that of H.E.S.S. in the same energy range. For energies in the neighborhood of 20 GeV the effective area is approximately 100 m^2 . At 1 TeV energies this increases to 10^5 m^2 and at 10 TeV energies this increases further to 10^6 TeV [47].

4. CTools Analysis Software

The present chapter provides a basic description of the CTools software package, version 1.5.2, which summarises the functionality of the software as a whole. Additionally, a list accompanied by an explanation of the executables implemented throughout this paper is also presented. Further details regarding the CTools methods and analysis techniques used may be found at <http://cta.irap.omp.eu/ctools/index.html>.

4.1 Overview

All analyses of astrophysical data throughout this paper make use of the CTools analysis software package. CTools is a software package specifically designed for the study and analysis of CTA data as well as existing event data from IACTs like H.E.S.S., MAGIC and VERITAS. Analysis of existing data may be performed on the condition that the data and response functions are in the format defined for CTA[15].

CTools may perform analyses on IACT event lists consisting of reconstructed event data which has been calibrated in energy and is of the DL3 data level. This data consists of only gamma-like events and the majority of the background have been removed. Instrument response functions (IRF) are also required in order to link physical photon properties with quantities of measured events.

CTools does support the analysis of data as well as IRFs from other gamma ray observatories, such as COMPTEL and Fermi-LAT; however, since this paper only deals with IACT data, only the associated IRF is discussed. In general, the IRF for

the analysis of IACT data is presented in the following form:

$$R(\mathbf{p}', E', t' | \mathbf{p}, E, t) = A_{eff}(\mathbf{p}, E, t) \times PSF(\mathbf{p}' | \mathbf{p}, E, t) \times E_{disp}(E' | \mathbf{p}, E, t) \quad (4.1.1)$$

The effective area, energy PSF and the energy dispersion are represented by A_{eff} , PSF and E_{disp} , respectively. The arrival direction, energy and time of the gamma ray photon is represented by \mathbf{p} , E and t respectively, where primed quantities indicate the reconstructed photon properties. The IRF is convolved with models, defined by 4.1.2, of gamma ray sources in order to obtain the probability density of events predicted by the model. These models may be factorised into a spatial, spectral and temporal component as displayed in equation 4.1.2:

$$M(x, y, E, t) = M_{spatial}(x, y | E) \times M_{spectral}(E) \times M_{temporal}(t) \quad (4.1.2)$$

where $M_{spatial}$, $M_{spectral}$ and $M_{temporal}$ represent the spatial, spectral and temporal models components, respectively.

Information regarding the IRF is stored in the form of a Flexible Image Transport System (FITS) file as a response table with multiple extensions representing the components of the IRF. Both the PSF and the energy dispersion are normalised and the PSF is defined by a sum of three 2D gaussian functions.

A CTool can be found as either a compiled C++ executable or as a Python script, termed *ctools* and *cscripts* respectively. In general, the python scripts are for complex, high-level tasks where various *ctools* are implemented, whereas the compiled *ctools* executables are intended to be used for basic analysis tasks[15].

CTools allows for a command line interface for a step by step analysis of the gamma ray emitting source under consideration. The Python modules declare each CTool executable as a separate Python class. Each CTool executes a well defined analysis task which allows for the production of a workflow, consisting of a combination of a number of CTools, that is specifically tailored to the analysis requirements

of the user[15].

The software allows for event simulation as well as comprehensive model fitting, providing the results in Extensible Markup Language (XML) format. CTools software also comprises various executables allowing for generation of binned data, spectra, light curves, residuals and images which are provided as FITS files on output. In order to graphically display the aforementioned outputs, CTools is accompanied by various Python plotting routines, which use matplotlib[15].

The software has been developed such that computations regarding spatial and spectral properties of a gamma ray emitter may be produced with a relative precision of less than 1%[15].

4.2 CTools and CScripts Used

The present section provides a brief description of all the executables used throughout this paper. Note that there are additional CTools and CScripts provided by the CTools software package that are not discussed. Only executables relevant to the study are presented. All facts regarding the CTools and CScripts presented in this section have been adapted from J.Knödlseder et al[15].

4.2.1 *ctobssim*

If actual event data is unavailable, in order to simulate events of a particular gamma ray source, *ctobssim* generates a simulated events list based on an initial source model and certain input parameters, such as radius of the field of view, pointing direction, energy thresholds, calibration database and instrument response function as well as a possible temporal component. The event list contains information regarding the arrival direction of gamma rays along with the associated energy.

An initial definition of the source and background is required in order to generate

the list of simulated events. This must be made available as an ASCII file in XML format which defines a model containing spectral, spatial and temporal information regarding the source under consideration, that is the gamma ray emitter, as well as an instrumental background model. The structure and contents of the input model definition file is shown in the appendix.

In order to perform a simulation for a given source, *ctobssim* utilises Monte-Carlo techniques. Each observation is assigned one random number generator with a seed parameter. Changing the seed value will result in a different set of simulated events, whereas leaving it unchanged will produce the same set of simulated events for repeatable simulations. For the purpose of this project, the seed parameter was set to a value of 1 where simulated events data was required. *ctobssim* makes use of these random number generators to produce random gamma ray events based on a model of the celestial gamma ray intensity distribution convolved with a certain instrument response function. In addition, *ctobssim* adds a number of random events to the events list based on the expected distribution of the residual background.

Only simulated events that fall within the specified energy range and region of interest will be saved to an output FITS file. The FITS file contains three extensions, an empty primary image extension, an extension containing all event information, such as pointing directions and associated energy, and an extension containing good time intervals.

Gamma ray events will be simulated in a cone-like shape with the radius and pointing direction specified at input. *ctobssim* will divide the energy range into energy slices. Events will be simulated for each energy slice and the simulation area will be modified to the effective area of the array for each energy interval. Thus, the overall results will be the sum of events from each energy slice. In addition, the photon rate and flux is also simulated for each slice.

4.2.2 *ctselect*

CTools allows for further cuts to be applied to both simulated and observed data which is provided in the event list format. The event list may be reduced to only consider events which satisfy certain criteria using *ctselect*. A time and/or energy constraint may be imposed on the event list or a certain circular acceptance region may be enforced. The executable will loop through all events, only saving those whose reconstructed arrival times, directions and energies meet the selection criteria. The output of selected events is saved in a FITS file.

4.2.3 *ctskymap*

A sky map of events may be produced by means of the CTool *ctskymap*. This executable takes in a list of events and will iterate through each event on the list and log each event as a count within a sky map based on the event energy and arrival direction.

The executable takes in various parameters at input regarding the specifics of generating the sky map. The executable will query a pointing direction as well as the energy interval one wishes to consider. In addition to this, the coordinate system and projection method are required. The size of the sky map, that is the area of interest, is also set at input along with the image scale, measured in degrees per pixel. Only events which fall within the pre-set energy interval and area of interest are considered. Additionally one may choose whether or not to exclude background contribution in the sky map, in which case a background model will be subtracted from the sky map.

The *ctskymap* executable offers three options for background subtraction. The option 'NONE' may be selected for the background contribution to be shown in conjunction with the source contribution.

If the IRF is available, the spatial and spectral templates found in the IRF may be used to remove the background contribution for the sky map. In this case, the background subtraction method should be set to "IRF".

If spectral and spatial background information isn't readily available from the IRF, the ring background subtraction method may be employed by selecting "RING" when queried for a subtraction method. This method centers an annulus around the source and estimates the background contribution from the annulus. The estimated background contribution is what is subtracted from the sky map. In order to obtain a reasonable background estimation, all areas of the sky map which provide a significant gamma ray emission, that is all sources, must be excluded when performing the subtraction. These exclusion areas may be supplied in the form of a ds9 region file on input.

4.2.4 *ctlike*

The spatial extent and position of a gamma ray source as well as the flux, spectral index and any additional spectral information may be determined by performing a maximum likelihood fit of a source model to the gamma ray source data. This task is carried out by the *ctlike* executable. Note that all likelihood fitting performed throughout this project was executed using *ctlike*.

ctlike adjusts the model parameters in an attempt to maximise the log-likelihood function for each observation. For the purpose of this paper, the Poisson log-likelihood function, given by equation 4.2.1, is implemented for all maximum likelihood fitting. Equation 4.2.1 is described by the difference in the number of events predicted by the fitted model for a given observation and the sum of the log of the probability density that given the fitted model, an event occurs.

$$- \ln L_i = \iiint P_i(\mathbf{p}', E', t' | M) d\mathbf{p}' dE' dt' - \sum_k \ln P_i(\mathbf{p}'_k, E'_k, t'_k | M) \quad (4.2.1)$$

Again, the arrival direction, energy and time of the gamma ray photon is represented by \mathbf{p} , E and t respectively, where primed quantities indicate the reconstructed photon properties. P_i represents the probability density. Essentially the log-likelihood function attempts to quantify the probability that the gamma ray data set obtained during a particular observation would occur given the fitted model. More on the log-likelihood value will be elaborated on in Chapter 5.

If multiple observations are taken then the negative log-likelihood value is summed over each observation in order to obtain a joint likelihood value.

The required input parameters include an event list of gamma ray source events, an initial source model to be fitted to the event data and, in certain cases, the IRF to be used as well as the calibration database. The executable will produce a XML file upon output containing the best fit parameter values of each model component that was fitted with the associated errors. Additionally, the test statistic, which will be elaborated on in Chapter 5, may be computed for a particular model component. The structure of the source model to be fitted is identical to that discussed in section 4.2.1. The difference in the number of observed events and the number predicted by the fitted model is also determined by *ctlike* as well as the covariance matrix associated with the fit.

4.2.5 *ctbutterfly*

The executable *ctbutterfly* produces a butterfly diagram for a specific source depending on the spectral model component. A butterfly diagram is an envelope of compatible models which are within a predetermined confidence limit.

Essentially, *ctbutterfly* divides the spectral energy range into a preset number of energy slices and determines the minimum and maximum spectral intensity, by means of gaussian error propagation, as well as the best fit intensity for each slice, from the fitted spectral model component produced by *ctlike*. *ctbutterfly* will accept

on input an event list of gamma ray events as well as the fitted model describing the gamma ray source and output a text file containing the aforementioned information.

A confidence limit of 68% was implemented for the entirety of this paper and for each butterfly diagram computed, 100 logarithmically spaced energy bins were implemented.

4.2.6 *csresmap*

A residual map is simply a sky map from which all fitted spatial model components are subtracted. This operation is carried out by *csresmap*. If not supplied, a model cube and a counts cube will be generated internally which are three dimensional data cubes that are spanned by right ascension, declination and energy.

The the event energy ranges of the cubes are divided into a predetermined number of bins with a specific spacing. Similarly, the right ascension and declination extents are divided into a number of bins of a particular size given in pixels. The fitted model is thereafter convolved with the IRF in order to obtain the event probability density for the fitted model. This probability density is then used for residual computation for each energy bin. Before the spatial residual computation may take place, the model and counts cubes are then collapsed into maps by summing over each of the energy bins. Various formulae are available for the computation of the spatial residuals.

For all spatial residual computations performed throughout the paper, 20 energy bins were used which are logarithmically spaced. In terms of the spatial bins, 200 linearly spaced bins with a 0.02 pixel extent were used. Additionally, the significance formula, given by equation 4.2.2, was implemented to generate the residual maps presented in this paper.

$$\delta = \text{sign}(M_{data} - M_{model}) \times \sqrt{2 \times (M_{data} \times \ln \frac{M_{data}}{M_{model}} + M_{model} - M_{data})} \quad (4.2.2)$$

The number of events predicted by the fitted model in each spatial bin is defined by M_{model} and the number of observed events defined within the event list for each spatial bin is given by M_{data} . The Signum function returns the sign of the difference between the number of observed events and that predicted by the model. This is performed on each spatial bin such that δ is obtained for each bin, essentially producing a matrix of residual values. The residual map is outputted as a FITS file.

4.2.7 *csresspec*

CTools possesses the ability not only to perform spatial residual computations but also spectral residual computations, which is carried out by *csresspec*. This executable follows the same principle for spatial residual computations. Again the energy range is divided into a predetermined number of energy bins with a specified spacing pattern and the probability density of the fitted model is used for the spectral residual computation for each bin.

The same number of energy bins as well as bin spacing used for spatial residual computations was applied for all spectral residual computations performed throughout this paper. Again the significance formula was implemented for spectral residual computations.

The output spectral residuals are written to a FITS file which contains the residual spectrum as well as the counts contribution of each gamma ray source component defined in the fitted model.

4.2.8 *csspec*

All spectral energy distributions were generated using *csspec* which divides the spectral energy range of a gamma ray emitter into a specified number of energy bins and

performs a maximum likelihood fit of the fitted model to each energy bin. From the resulting fit, the best fit source flux is calculated for each bin as well as the error associated with the flux. The test statistic may also be computed for each energy bin as well as the flux upper limit. In the case where source events are not significantly detected in a certain energy bin, the flux upper limit is taken as the flux for that particular energy bin.

For all spectral energy distributions presented in this paper, 10 energy bins were implemented which are logarithmically separated. The resulting distribution is outputted as a FITS file.

4.2.9 *csiactdata*

The present CScript accepts the path to the directory where the data stored as FITS files is located. *csiactdata* inspects the directory and outputs the data sets available. Each data set is assigned a unique name and is stored according to the storage conventions of IACT data. The data is stored as several FITS files with each FITS file representing one observation.

4.2.10 *csfindobs*

In order to sort through the numerous FITS files *csfindobs* selects the observations within the FITS data set which are within the radius of interest of the pointing direction. This executable generates a list of observation IDs which share common properties, such as pointing direction, zenith angle, source identity as well as observation time, in an ASCII file format.

4.2.11 *csiactobs*

The list of runs generated by *csfindobs* needs to be converted to a single observation definition file containing information regarding the event list, energy dispersion, PSF and effective area associated with each observation in order to be usable for general data analyses. This is performed using *csiactobs*. Additionally, this executable generates a separate observation definition file containing separate background models for each observation within the run list. Examples of the structure of the observation definition file is found in the appendix. The background model file follows the same format as that of the model definition file.

4.2.12 *csmodelmerge*

The present executable possesses the ability to combine several models, in the form of model definition files into a single model XML file.

5. Analysis Criteria

The present chapter details the analysis criteria implemented in order to evaluate the sensitivity of CTools to resolve two sources and to detect a cut-off energy for a CTA data set as well as to determine the most appropriate spectral and morphological models of two gamma ray emitters in the LMC, namely N 157B and 30 Dor C.

5.1 Overview

In general, the analyses in the forthcoming chapters deal with comparing the log-likelihood values of the fit of test models, which have been fitted to either simulated or observed data, and comparing the quality of the fits by means of p-value and significance calculations. In particular cases both spatial and spectral residuals in conjunction with best-fit model parameter values will be assessed.

5.2 Log-Likelihood Values

The test models consist of a simple null model, or hypothesis, of the data set and at least one parameter-rich alternative model. Intuitively, the parameter-rich alternative models will always be a better representation of the data as a result of the additional parameters. Therefore, the log-likelihood values, that is the value outputted upon performing a maximum likelihood fit of the test models to the data, of the fitted alternative models will be larger than that of the null model. It follows that even if the alternative model is not a better description of the data than the

null model, the log-likelihood value will be greater than that of the null model. The alternative model would then have to produce an increase in the log-likelihood value greater than the increase associated with the additional degrees of freedom for it to be considered a better representation of the data than the null model. This increase may be quantified by the p-value associated with the difference in the log-likelihood values between the null and alternative models.

5.3 P-Values

Further analysis of the log-likelihood values was implemented by calculating the p-value associated with a given pair of test models being compared. Generally, the p-values were calculated between the null model and each alternative model. The p-value is a measure of the extent to which the null model describes the observed data. It is a representation of how likely an observed data set is better represented by a null model, rather than a more complex alternative model.

The principle for determining the p-value between two models makes use of Wilks theorem[48]. Wilks theorem states that the likelihood ratio of two models of a given large data set asymptotically approaches a χ^2 distribution when one model is contained within the other [48]. More concretely, given an initial model θ_0 , of a given large data set, whose parameter space forms a subset of that of an alternative model θ , the likelihood ratio may be calculated as follows:

$$\eta = -2\ln \frac{L_{\theta_0}}{L_{\theta}} \quad (5.3.1)$$

where L_{θ_0} and L_{θ} are the log likelihoods of the two models, respectively, and η is an indication of how well the data is supported by the initial model. As the size of the data set approaches infinity, the probability density function (pdf) of η will follow a χ^2 distribution with N degrees of freedom, where N is the difference in the degrees of freedom of the two data models. That is to say:

$$pdf(\eta) \sim \chi_N^2 \quad (5.3.2)$$

Integrating over the pdf with respect to η will yield the p-value which quantifies the compatibility between data set and the initial model. All p-value calculations made henceforth will make use of Wilks theorem, whose implementation is possible due to the sizable data sets dealt with and the fact that the parameters of the models under comparison are subsets of the most parameter rich model in the respective comparisons.

A lower p-value suggests strong evidence that of the two models being compared, the parameter-rich alternative model is a better representation of the data set. More concretely, a smaller p-value implies that the observed data is unlikely if the null model is considered to be true. Conversely, a larger p-value is indicative that the alternative model provides no significant improvement over the null model's description of the data set. While a magnitude comparison of p-values does give an indication as to which of the test models the data set favours, a threshold value below which the null model is rejected and an alternative is accepted is necessary. This requires the calculation of a p-value's associated significance.

5.4 Significance

A definite acceptance/rejection criterion is needed in order to narrow down the test model which best describes the data set. This criterion was chosen to be a confidence interval at a significance level of 5.3σ corresponding to a p-value of 10^{-7} . That is to say that if a p-value is to fall below this threshold of 10^{-7} or have an associated significance of greater than 5.3σ , it is highly unlikely that the observed data could be reproduced if the null model is assumed to be true. It follows that there is reason to assume that the alternative model is better in describing the data set.

6. Sensitivity Analysis on Simulated Data

In this chapter, the sensitivity of CTools in conjunction with the IRF to detect a cut-off energy of a source will be explored in addition to CTools' ability to disentangle confused sources. A modified simulated CTA data set of the Crab Nebula was used as the application domain for this stage of the research.

In order to determine the degree of resolution of CTools, We produced a Python analysis pipeline which has the capability to fit various source models, iteratively, to a simulated data set based on an initial input model.

The degree of sensitivity of the CTools software in analysing a CTA data set was determined by considering log-likelihood values as well as additional statistics such as p-values and significance.

6.1 Analysis Pipeline

In general, the pipeline will generate a list of simulated events based on an initial input model. The pipeline will then attempt to fit up to two test models, that is a null model and a parameter rich alternative model, containing both spatial and spectral information regarding a source, to the event list and output the maximum log-likelihood and best fit parameters for each fit. The pipeline is also capable of assessing the goodness of fit of the two models to the data by determining the p-value (which may be as expressed as a significance value) using the test statistic, which

depends on the ratio of the maximum likelihood of the two fits.

Furthermore, the pipeline has the ability to iteratively change the parameters of the input model as well as the two test models and perform successive fits to the new event list. It follows that successive maximum log-likelihood, p-value and significance calculations and comparisons are possible which allows for one to observe the trend of the p-values with a change in a particular parameter value. Residual and spectral computations are also possible.

We used simulated CTA event lists of the Crab nebula to assess the sensitivity. The input models and initial parameter values used to generate the event lists are modified versions of the Crab Nebula initial source model supplied by the CTools package.

6.2 Cut-off Energy Sensitivity

The cut-off energy of a particular source is the energy at which the spectrum deviates from the expected trend. More specifically, it is the energy at which the spectrum of the source begins to decrease faster as a function of energy than its functional form at lower energies. Identifying the position and shape of the cut-off of a source may impart vital information regarding the particle acceleration mechanisms and energy loss rate of a particular source[49] as well as emission processes[50]. The spectral energy distribution for this particular energy range, that is the gamma ray energy regime, is dominated by inverse Compton emission from the gamma ray emitter.

Efforts have been made by Romoli et al[49] in improving the sensitivity to identify various cut-off parameters. While this paper focuses on software sensitivity, Romoli et al[49] focuses rather on instrumental sensitivity. They planned to increase the effective area of a given gamma ray instrument by lowering the energy threshold of ground based Cherenkov telescopes in order to more sensitively identify

cut-off parameters within the cut-off region. Ultimately, it was found that parameters regarding the cut-off region of a source could be determined with a reduced uncertainty of approximately 10%.

The present section evaluates over which energy range CTools is able to detect a cut-off energy. Varying spectral models with a cut-off do exist. However, for the purpose of this paper, the simplest form of an energy spectrum with a cut-off will be used, that being an exponentially cut-off power law. Further particulars regarding this spectral model are discussed in the proceeding sections.

6.2.1 Description of Initial Model Components

In assessing the ability of CTools to detect a cut-off, the Crab Nebula spectrum was described by a power law with an exponential cut-off to the same order of that determined by Aharonian et al[22], 14.3 TeV, as previously described in Chapter 2.

With this in mind, the pipeline proceeded to generate an event list of simulated events of the Crab Nebula from an initial source model, which defines the Crab spectrum to follow a power law with an exponential cut-off of 10^6 MeV. Thus, the spectral component of the model will implement the following:

$$\frac{dN}{dE}(E) = k_0 \left(\frac{E}{E_0} \right)^\gamma \exp \left(\frac{-E}{E_{cut}} \right) \quad (6.2.1)$$

where k_0 is the prefactor, or the normalisation constant. The prefactor is the differential flux at an energy E_0 ($\text{ph.cm}^{-2}.\text{s}^{-1}.\text{MeV}^{-1}$). The value E_0 , set to 0.3×10^6 MeV, is the pivot energy which serves as a normalisation point. The spectral index of the celestial object under consideration is given by γ . Lastly, the cut-off energy is defined as E_{cut} . In general, the power law component of equation 6.2.1 is dominant at higher cut-off energies, whereas the exponential component dominates at lower cut-off energies.

The Crab Nebula's morphology was approximated as a point source; thus, the spatial component consists of a single spatial point. All spectral parameters are free with the exception of the pivot energy.

Two additional test models, that are to be fitted to the data, are required to assess the cut-off sensitivity. The first model fitted hypothesises the Crab spectrum to follow a power law relation with the following spectral component:

$$\frac{dN}{dE}(E) = k_0 \left(\frac{E}{E_0} \right)^\gamma \quad (6.2.2)$$

This model will be taken as the null hypothesis, H_0 .

The alternative model, termed H_1 , hypothesises the Crab spectrum to follow a power law with an exponential cut-off at 10^4 MeV and will implement a spectral component identical to that of equation 6.2.1. This model to be fitted is identical to the initial source model used in producing the events list. Table 6.2 describes the model parameters used for the initial source model, the cut-off model (H_1) as well as the power law model (H_0).

Table 6.2: A table showing the initial parameter values of each model, that is, the source model, the cut-off model and the power law model.

Model Parameters	Initial Source Model	Power Law Model (H_0)	Cut-Off Model (H_1)	Spectral Component of Background Model
Right Ascension ($^\circ$)	83.63	83.63	83.63	N/A
Declination ($^\circ$)	22.01	22.01	22.01	N/A
Prefactor ($\text{ph.cm}^{-2}.\text{s}^{-1}.\text{Mev}^{-1}$)	5.7×10^{-16}	5.7×10^{-16}	5.7×10^{-16}	1
Spectral Index	-2.50	-2.50	-2.50	N/A
Pivot Energy (MeV)	0.3×10^6	0.3×10^6	0.3×10^6	10^7
Cut-off Energy (MeV)	10^6	N/A	10^6	N/A

The initial parameter values for the background component of all three models is also contained within Table 6.2. The background component for all models is

derived from the information regarding the instrumental background contained in the IRF.

It can be seen that the background model also contains spectral information. The CTA instrumental background model was used which consists of a template which predicts the background rate in units of $\text{events}\cdot\text{s}^{-1}\cdot\text{MeV}^{-1}\cdot\text{sr}^{-1}$ based on the position within the field of view as well as the measured energy. The spectral component defined in Table 6.2 will only come into effect when it is multiplied by the CTA instrumental background model where spectral adjustments regarding the energy distribution of the background rate need to be made.

It can be seen that in Table 6.2, the power law is set to a value of one, making the complete background model simply the instrumental background from the IRF. The power law will only come into effect when model fitting takes place where spectral adjustments need to be made.

Note that the prod2 calibration database was used with the South 0.5h IRF which was included in the CTools software package and was the newest IRFs available at the time of testing. The Southern array was used with the expectation of a better angular resolution which would aid in the purpose of the analysis. An observation time of a few hours is sufficient for studies of the Crab Nebula given its brightness, hence the use of the 0.5h IRF. This configuration allows for a total of approximately 200000 predicted events.

6.2.2 Methodology

The pipeline proceeded to perform a maximum likelihood fit of the spectral properties to the event list of both the null and alternative model. The p-value is determined by comparing the log-likelihoods of the fits of the two test models by means of invoking Wilks theorem[48]. The program repeated this procedure while iteratively increasing the cut-off energy of both the source model and the cut-off model in a

preset step size. As previously mentioned, the start value of the cut-off energy was set to 10^4 MeV. The upper limit for which a cut-off energy was tested for was 10^8 MeV.

Considering the analysis plan described in Chapter 5, the trend of the p-values with an increasing cut-off energy was determined. It follows that a lower p-value at a particular cut-off energy would suggest strong evidence against the null model, in which case would suggest that the alternative model better represents the data, showing evidence for a cut-off at that energy. Alternatively, greater p-values suggest that the simulated data favours the null model indicating the failure of the algorithm to detect a cut-off at that energy. The significance level defined in chapter 5 was applied as the threshold and was used to determine the interval over which CTools is able to detect a cut-off energy.

Several other parameters were also looked at when inspecting the cut-off sensitivity. The true cut-off energy, that is the cut-off energy defined within the simulated data set, was compared to the best fit values of the cut-off energy from the alternative model. If the algorithm succeeded in finding a cut-off, then there should be a strong correlation between the fitted and true cut-off energy values.

The best fit values of the spectral indices of both the null and alternative model were compared to the true cut-off energy. In theory the best fit spectral indices should lie within the neighbourhood of -2.50 since this is the value defined within the event list.

The error associated with the aforementioned best fit values were also taken into consideration.

6.2.3 Results

The tests and assessments used in assessing the ability of CTools to detect a cut-off energy are presented in the proceeding sections. Figure 6.2 summarises the results

of the trends of the p-values along with the fitted cut-off energies and fitted spectral indices in regards to the cut-off energy of the simulated data set. The application domain of cut-off energies ranged from 10^4 MeV to 10^8 MeV. Errors in the best fit parameter values were several orders of magnitude (10^5 to 10^{19}) larger than the fitted values for the range 10^4 MeV to 10^5 MeV which distorted the trends of the results. With the p-values obtained for the fitted parameters in this range being greater than the threshold of 10^{-7} , it may be concluded that the null model is a better representation of the data and ;thus, the results for this energy range were omitted. Therefore, only results where the cut-off energy lies in the range 10^5 MeV to 10^8 MeV are presented, where best fit parameters are dealt with.

6.2.3.1 P-Values and True Cut-Off Energy

Figure 6.2a depicts the dependence of the p-values of each fit on the true cut-off energy. Although there are fluctuations present throughout the energy range, the general trend of the graph is apparent. The p-values steadily decrease up until the point at which the cut-off energy is in the neighbourhood of 10^6 MeV. Thereafter, the graph begins to steadily increase again. The fluctuations present throughout figure 6.2a are a result of statistical fluctuations of fitting the models to the simulated data.

Applying the threshold described in Chapter 5 it can be seen that the p-values hit the threshold of 5.3σ , or 10^{-7} , at a cut-off energy of approximately 1.43×10^5 MeV and again at 1.20×10^7 MeV. Thus, the algorithm is able to find a cut-off energy which lies in the range 1.43×10^5 MeV to 1.20×10^7 MeV. A cut-off energy which is not situated in this range will not be detected by the algorithm or the CTA instrument. Note that the former lower and upper energy limits were determined by considering the midpoint of the portions of the graph which strike a p-value of 10^{-7} . Figure 6.3 depicts this finding more clearly.

As previously stated, figure 6.3 reaches a minimum in the neighbourhood of 10^6 MeV. This implies that the simulated data set is best represented by the alternative

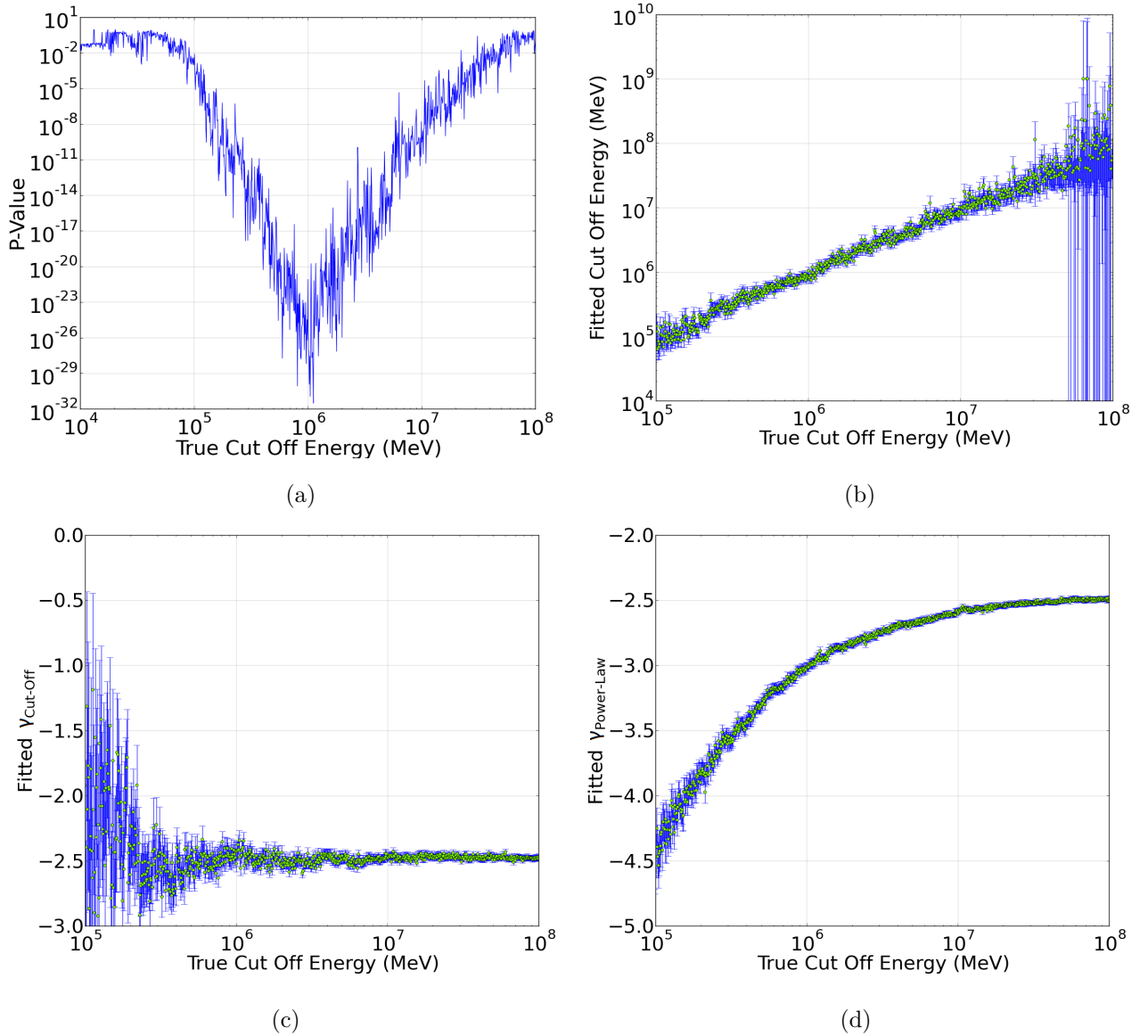


Figure 6.2: Graphs showing the results from cut-off sensitivity tests. Figure (a) shows a log-log plot of the p-value trend with various cut-off energy values. Figure (b) displays a log-log plot comparing the best fit cut-off energy values to the true cut-off energy value. Semi-log plots of the fitted values of the spectral indices are shown for (c) the cut-off model and (d) the power law.

model, H_1 , in the neighbourhood of 10^6 MeV, therefore, the algorithm is most susceptible to detect a cut-off energy in the vicinity of 10^6 MeV.

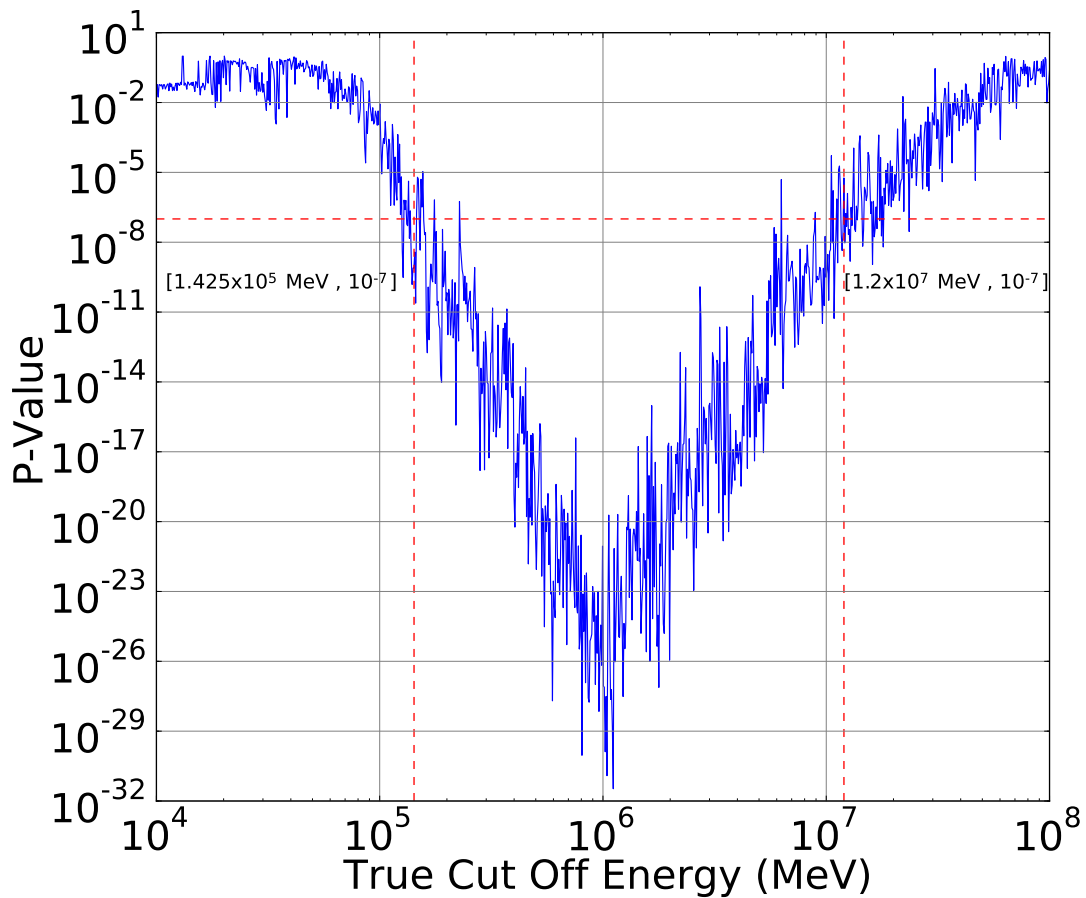


Figure 6.3: A log-log plot showing the trend of the p-values with a change in the true cut-off energy. The threshold of 5.3σ is reached at a cut-off energy of 1.43×10^5 MeV and once again at 1.20×10^7 MeV. It follows that the software is able to find a cut-off energy in the range 0.14 TeV to 12 TeV.

6.2.3.2 Fitted Cut-Off Energy and True Cut-Off Energy

Figure 6.2b displays the relationship between the true cut-off energy and the best fit values when fitting H_1 to the simulated data defined in the event list. Towards the upper limit of the energy range, greater than 10^7 MeV in the vicinity of 10^8 MeV, the p-values lie above the acceptance threshold of 5.3σ , where the alternative model is rejected and the null model is accepted. Thus, the algorithm was unable to detect a cut-off in the neighbourhood of 10^8 MeV. The reason for this is that at higher cut-off energies the power law term in equation 6.2.1 dominates the spectrum and, thus, the algorithm is unable to accurately fit the exponential term to the sim-

ulated data, since it cannot determine a cut-off energy. It follows that these energies were disregarded as possible values of a cut-off energy. It is more likely that the data is described by the alternative model within the energy range of 10^5 MeV to approximately 7×10^7 since the p-values lie below the threshold within this energy range. Thus, only energies between 10^5 MeV and 7×10^7 were considered. This is in agreement with the findings of section 6.2.3.1.

Considering the aforementioned energy range the error bars associated with the fitted cut-off energy are approximately uniform, of the order of 10^4 MeV, within the energy range. For this energy range it appears that the data shows a linear correlation with a correlation coefficient of 0.98, indicating a strong positive linear correlation with little noise. Upon calculating a regression line by means of least squared regression, a slope of 0.93 ± 0.02 with an intercept of $(9.4 \pm 6.0)10^4$ TeV was produced. The expected value of the slope is 1 and that of the gradient is 0 since that would imply that the fitted values of the cutoff energy is the same as the true values. The slope is within 3.5 standard deviations from the expected value of 1 while the intercept is within 1.6 standard deviations of the expected value of 0. Given this finding, the alternative model is an accurate representation of the simulated data set within the energy range of approximately 10^5 MeV to 7×10^7 MeV, therefore, the software succeeded in detecting a cutoff energy.

6.2.3.3 Fitted Spectral Indices and True Cut-Off Energy

Figures 6.2c and 6.2d depict the change in the fitted spectral index of H_1 and H_0 with a change in the true cut-off energy, respectively.

Looking at figure 6.2c the fitted spectral indices of H_1 generally lie within the neighbourhood of $\gamma = -2.50$, which is expected since the spectral index defined within the initial source model used to generate the simulated data was set at $\gamma = -2.50$. This is an indication that the alternative model is a fair representation of the simulated data set. There is, however, a large dispersion of the data points for lower cut-off energies with large associated errors, up to 16 orders of magnitude

greater than the fitted values. The reason for this is that at lower cut-off energies the exponential term in equation 6.2.1 overwhelms the power law term, resulting in the algorithm being unable to observe the power law component and, thus, the spectral index is unable to be accurately fitted.

Figure 6.2d shows the fitted spectral indices of H_0 in conjunction with the true cut-off energies. The spectral indices appear to steadily increase, from a value in the proximity of -4.5, as the true cut-off energy increases and finally plateaus to a value of approximately -2.50 for higher cut-off energies.

The reason for the varying spectral indices for lower cut-off energies is that, as before, at lower cut-off energies the power law component becomes negligible. It follows that the algorithm will be unable to find the power law component of the spectrum and incorrectly fit the null model. In other words, when fitting a power law spectrum to the simulated data, at lower cutoff energies the algorithm will attempt to fit a power law spectrum with a lower spectral index in order to account for the low cutoff. Graphically, this is displayed in figure 6.4 where a semi-log plot has been generated for an energy range of 10^{-4} TeV to 100 TeV for demonstration purposes only.

The solid and dashed dark blue plots represent power laws with a spectral index of -2.5 and -4.5, respectively. The remainder of the plots represent exponentially cut-off power laws with a spectral index of -2.5 and cut-off energies ranging from 10^{-4} TeV to 100 TeV. As the cutoff increases less of the power-law spectrum lies past the cut-off energy. As a result the best fit value of the spectral index of the power-law spectrum is flatter for higher cut-off energies since a power law spectrum with a fairly high cut-off energy, that is a 'soft' cutoff, deviates only slightly from a regular power law spectrum. In this case the power law component dominates over the exponential component making the deviation from a pure power law minute. It is for this reason that at higher cutoff energies the spectral indices in Figure 6.2d converge in the neighbourhood of -2.50.

For lower cut-off energies the best fit value of the spectral index is steeper since more of the power-law spectrum lies beyond the cutoff. A steeper spectral index is fitted to accommodate the hard cutoff. Taking this into consideration, even though the associated errors are small, in the range of 10^{-1} to 10^{-2} , the null model is not an entirely accurate representation of the simulated data for lower cut-off energies. This is so because a substantial deviation in the spectral index from -2.50 indicates a different source optical density to that defined within the simulated data, giving false information regarding the emission mechanism of the source.

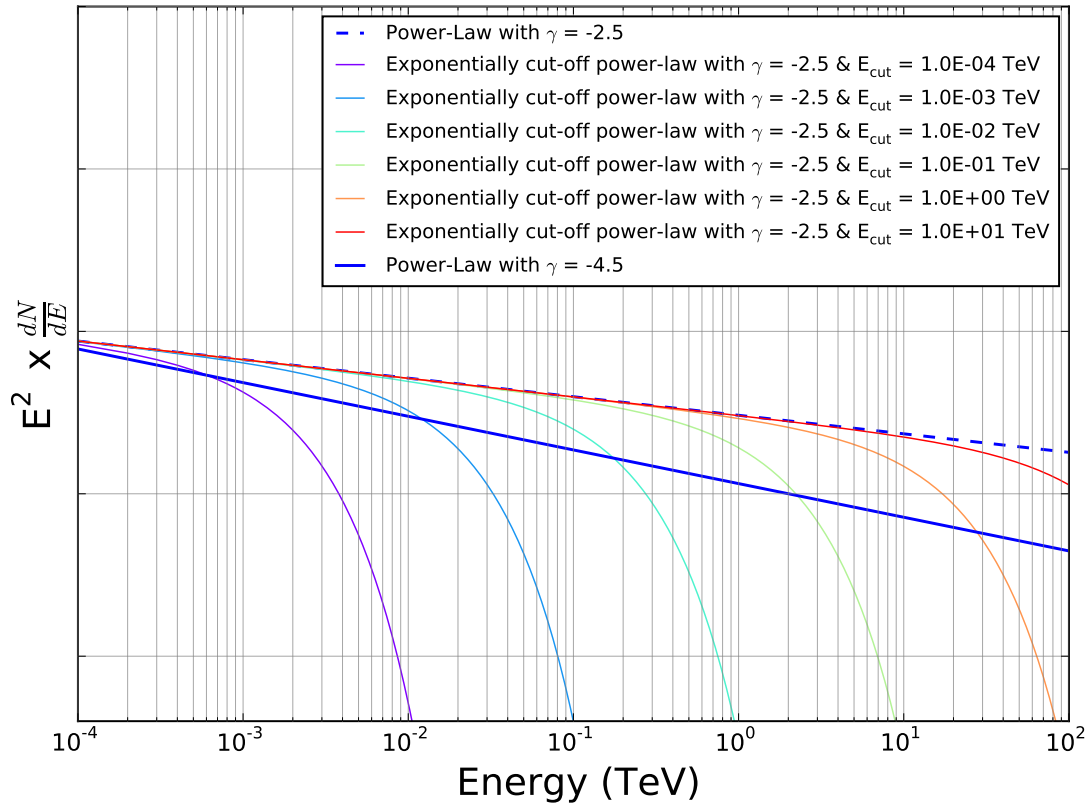


Figure 6.4: A graph underlining the reason for a varying fitted spectral index for lower cut-off energies when fitting the null, power law, model to the simulated data. The plot shows that for high cut off energies, the power law component is dominant over the exponential component and, in turn, demonstrates that at lower cutoff energies the exponential component is dominant.

6.3 Disentangle Confused Sources

Confused sources are categorised as sources which are unable to be resolved as a result of small off-set angles or contamination of one source by a close neighbour. Being able to disentangle confused gamma ray sources in a data set would be vital in identifying previously unknown gamma ray emitters which could serve as subject for further studies.

The present section evaluates the ability of CTools to not only resolve two closely situated gamma ray sources, that is sources with small angular separations, but also resolve two sources in the case of one source being completely "out-shined" by a brighter companion source.

6.3.1 Description of Initial Model Components

The procedure for evaluating the ability of CTools to resolve two sources is similar to that used in section 6.2. It was assumed that the Crab Nebula may be described by a power law in the energy range 0.1 TeV to 100 TeV. It was further assumed that there is an additional, much dimmer gamma ray source within the vicinity of the Crab Nebula.

Based on this assumption the pipeline generated an event list from an initial source model with two sources present, that is, the Crab Nebula and a pseudo source with a brightness that is 10% that of the Crab Nebula. The pseudo source, like the Crab Nebula, is described by a power law in the form of equation 6.2.2, however, the prefactor is 10% that of the Crab Nebula. For the time being both the Crab Nebula and the pseudo source will have the same declination and right ascension, therefore, the pseudo source will be completely enveloped by the Crab Nebula. Both sources will be modelled as point sources.

As before, two additional test models are required. Thus, it follows that one

model, the null model (H_0), assumes the Crab Nebula to be the only source contributing to the event list, whereas the alternative model (H_1) suggests that a pseudo source in conjunction with the Crab Nebula contributes to the event list. Again, the alternative model is identical to the initial source model. Both the null and alternative model assumes the Crab Nebula and the pseudo source to be point like sources with power law spectra. Again, the power law implemented is of the form described in equation 6.2.2.

Table 6.3 describes the initial model parameters used for the initial source model as well as the null and alternative model. Information regarding the background contribution for all three models is also present in the table. The background is modelled as a power law as in section 6.2. The prod2 calibration database was used, as in Section 6.2, with the South 0.5h IRF.

Table 6.3: A table showing the initial parameter values of each model, that is, the source model, the single source model and the multiple source model.

Model Parameters	Initial Source Model		Single Source Model (H_0)	Multiple Source Model (H_1)		Background Model
	Crab Nebula	Pseudo Source	Crab Nebula	Crab Nebula	Pseudo Source	
	Right Ascension ($^\circ$)	83.63	83.63	83.63	83.6	
Declination ($^\circ$)	22.01	22.01	22.01	22.01	22.0	N/A
Prefactor ($\text{ph.cm}^{-2}.\text{s}^{-1}.\text{MeV}^{-1} \times 10^{-16}$)	5.7	0.57	5.7	5.7	0.57	1
Spectral Index	-2.50	-2.50	-2.50	-2.50	-2.50	0
Pivot Energy (MeV)	10^6	10^6	10^6	10^6	10^6	10^7

6.3.2 Methodology

Both the null and the alternative model were fitted to the event list by means of a maximum likelihood fit of spectral and spatial properties, which was carried out by the pipeline. The source positions were fixed while spectral properties, the prefactor and spectral index, were left as free parameters during modeling process. The position of the pseudo source in the alternative model was fixed to be the same as that of the true direction of the pseudo source defined in the initial source model. The

position of the Crab Nebula was fixed to be the same as the true direction defined in the initial source model for both the null and alternative models.

Again, the p-values were determined from the log-likelihoods of the two fits by means of Wilks theorem [48], where the p-values describe probability that the data may be described by the null model. The program repeated this process while iteratively increasing the offset of the pseudo source from the Crab Nebula for both the source and alternative model. That is, the declination of the pseudo source was increased in a predetermined step size from a 0.0° offset to a 1.0° offset while performing a likelihood fit of the two models with each iteration.

The ability of CTools to resolve two sources were evaluated by observing how the p-values change with an increasing offset. The significance level of 5.3σ from Chapter 5 was once again taken as the threshold, meaning that if the p-values drop below approximately 10^{-7} , there is strong evidence to suggest the null model to be inaccurate and for the alternative model to better fit the data. Therefore, the offset at which 5.3σ is exceeded is the offset at which the software begins to resolve two entangled sources.

6.3.3 Results

In general, for higher offset angles, the alternative model provides a higher probability of producing the simulated data compared to the null model. This is to be expected since the null model only accounts for a single source. Figure 6.5 clearly depicts the trend of the p-values in regards to an increasing offset angle.

For an offset angle of up to 0.02° the p-values reach approximately unity, meaning that there is weak evidence for any increased probability of the alternative model producing the data compared to the null model. This suggests that the algorithm is unable to resolve two sources at such small offset angles. Thereafter the p-values sharply decrease and begin to plateau.

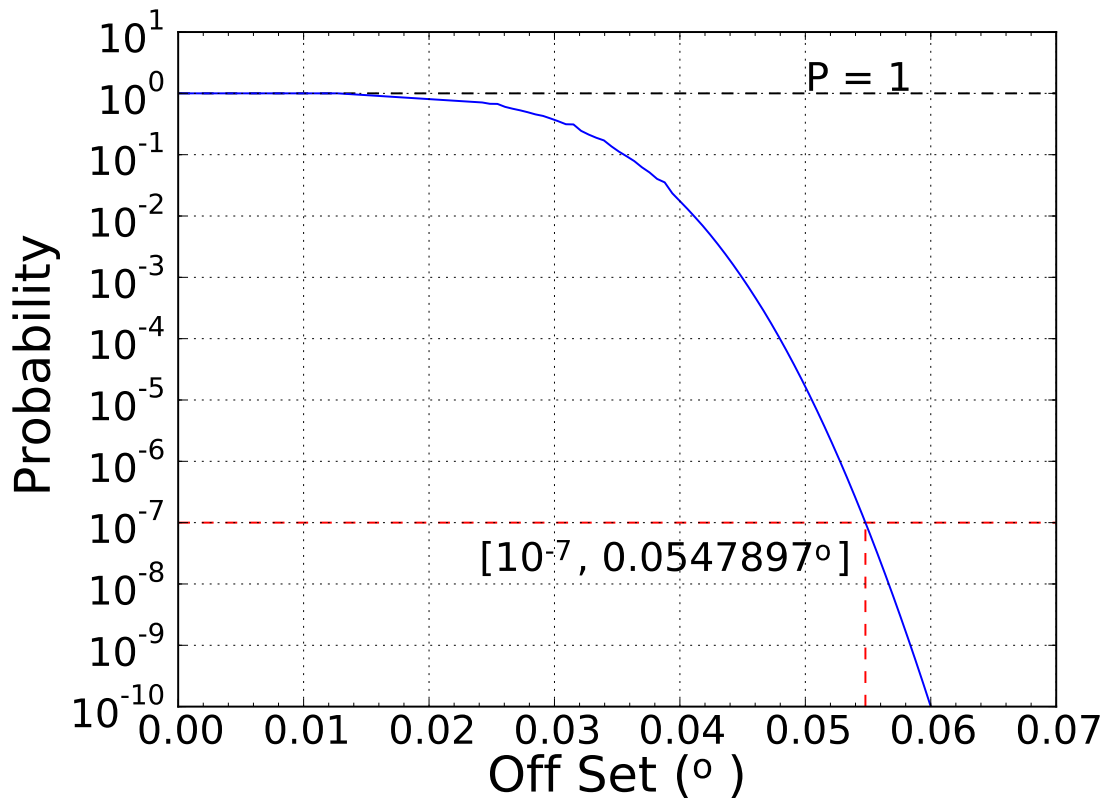


Figure 6.5: The graph depicts the p-Value change with an offset angle 0.07° . It is shown that at an off-set angle of 0.05° the threshold of 5.3σ is reached, indicating that the algorithm is able to resolve two sources from an off-set angle of approximately 0.05° .

The chosen threshold was 5.3σ , corresponding to a p-value of 10^{-7} , for 1 degree of freedom, specifically a fixed, known position and a free, unknown spectrum. This threshold was reached when the pseudo source is offset by 0.05° from the Crab Nebula, as depicted in Figure 6.5. Thus, for offset angles greater than 0.05° , the alternative model containing two sources is a better representation of the simulated data than the null model. It follows that the software is successful in resolving two sources provided their angular separation is a minimum of 0.05° . An offset smaller than this minimum angle will result in failure of the algorithm to disentangle two nearby sources.

Figure 6.6 shows a sky map of the two sources at a 0.05° offset, that is, the offset at which CTools is able to resolve the two. The pseudo source is present in the sky map, however, it is indistinguishable from the Crab Nebula. Even though the

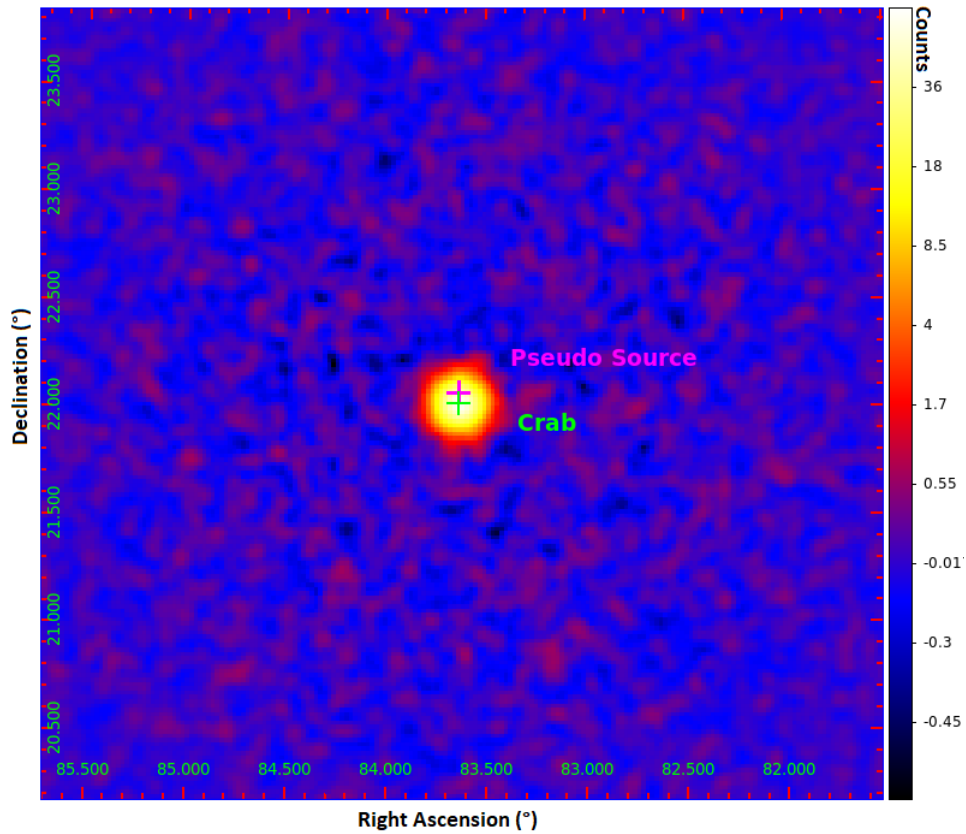


Figure 6.6: The sky map displays a $4^\circ \times 4^\circ$ region of the sky centred on the Crab Nebula with the pseudo source off-set by 0.05° . The pseudo source is present in the sky map, however, it is completely outshined by the Crab Nebula. An IRF background subtraction was applied to the sky map.

software is able to resolve the two sources at this offset, it is not visually apparent that two sources are present, due to the pseudo source being much fainter than the Crab Nebula. Therefore, the CTools software is able to not only spatially disentangle sources from an offset angle of 0.05° , but also resolve sources in terms of their spectra in cases where a source outshines a much fainter neighbour. This result applies to the Crab Nebula observed for 0.5 hours by the CTA Southern array in the prod2 configuration with a secondary source 10% of the flux of the Crab Nebula with a spectral index the same as that of the Crab Nebula.

The purpose of this work is to study how nearby sources can be separated and how the sensitivity can be quantified. The study was done with the example of the Crab Nebula and a pseudo source with a flux of 10% of the Crab. The result is

expected to depend on the fluxes and spectral indices of the gamma-ray sources, as well as the observation times and instrument configurations. Further studies in this direction is needed when applying this finding to other types of sources observed under different conditions.

6.4 Conclusion

For both sensitivity analyses conducted in this chapter, the prod2 calibration database was used in conjunction with the South 0.5 IRF. In total this configuration predicted approximately 200000 gamma-ray events.

For this configuration success was achieved in determining the lower and upper limits for which a deviation in the power law spectrum of the Crab Nebula, namely the position of a cut-off energy, may be detected by CTools for a CTA data set, that is, gamma-ray events in the energy range 20 GeV to 300 TeV. Additionally, the minimum offset angle for which two gamma-ray sources, specifically the Crab Nebula and a secondary source with a flux 10% of that of the Crab Nebula, may be resolved by CTools for a CTA data set was also successfully determined.

The software was able to position the cutoff energy of a gamma ray source within a CTA data set within the energy range of 0.14 TeV to 12 TeV with a 5.3σ significance. The analysis was also able to spatially distinguish two CTA sources up to an off-set of 0.05° while simultaneously fitting the spectra of the two sources in the case where contamination from the neighbouring source is a factor. This was again achieved with a 5.3σ significance.

It follows that the CTools analysis software was successfully applied to a specific configuration of simulated CTA events of the Crab Nebula where the respective sensitivity, dependent on both the software and IRF, regarding spectral and spatial resolution was evaluated. The cutoff-detectable energy range and the minimum detectable offset of these sensitivity studies would change with various configurations

of source fluxes and spectral indices, as well as observation times and instrument configurations. Further studies in this direction is needed in order to determine how changing these parameters would influence the sensitivity results.

The proceeding chapter advances this study by applying the CTools analysis framework to an existing H.E.S.S. data set of the gamma ray emitters N 157B and 30 Dor C, where the ability of CTools to spatially resolve two sources while simultaneously fitting the spectra and morphologies will be assessed where contamination of a source by its neighbour and the background is a factor.

7. Analysis of H.E.S.S. Data

Thus far, the capabilities and applications of CTools have been explored and the sensitivity evaluated on simulated CTA data of the Crab Nebula. It has been established that CTools has the ability to disentangle confused sources, from an off-set of 0.05° , and detect a cut-off energy, in the approximate range of 0.14 TeV to 12 TeV for a CTA data set, which involves model fitting, residual inspection as well as event simulation and selection.

The present chapter evaluates the CTools software on real data, namely data from H.E.S.S. observations of the LMC. That is to say, the ability of CTools to spatially resolve two sources and to determine the spectral energy distribution of two sources simultaneously is now being applied to real data to determine how it fares. The sources studied in this chapter includes the PWN N 157B along with the superbubble 30 Dor C.

Since the aim of this paper concerns the separation of two closely situated and confused sources, only high resolution H.E.S.S. data was dealt with as opposed to standard, loose or faint data. One of the benefits of using the high resolution data over the other data sets would be the improved angular resolution which is better suited for morphological studies. However, the total number of events within the high resolution data would be less than that of the other data sets which could be problematic for fainter gamma-ray sources if a well-characterised PSF is used.

The high resolution cuts were produced by a method developed by de Naurois and Rolland[51] which involves comparing the images produced from Imaging

Atmospheric Cherenkov Telescope cameras with model predictions by means of a log-likelihood minimisation algorithm.

The morphology of 30 Dor C was determined by evaluating several different morphological models and comparing not only the maximised log-likelihood values of each of the fits, but also the significance as well as the residuals. Once a morphology was determined for 30 Dor C, the spectrum of N 157B was deduced by fixing all morphological parameters and fitting various spectra to data. The spectrum was again determined by means of likelihood, significance and residual comparisons.

7.1 Data Preparation and Reduction

Unlike previous sections, no initial source model was required to generate a simulated events list, as real data from H.E.S.S. is dealt with. Instead, the H.E.S.S data comprises several unique runs with associated event lists and IRF details stored as FITS files. The data set consists of gamma ray events from and surrounding the 30 Doradus region. This region was observed for a total of 210 hours by H.E.S.S.

From the available FITS data, only observation runs which fall within a 2.0° radius around N 157B were chosen and used to assemble a more specific list of runs in ASCII file format. In total, 471 unique observation runs were selected, consisting of 56438 gamma ray events.

Thereafter, all relevant runs were compiled into a single observation list, that is, an observation definition XML file containing information regarding the event list, energy dispersion, PSF and effective area associated with each run. Additionally, an observation definition XML file containing individual background models for each run within the observation list was generated.

Further cuts were applied to the data in order to select runs contained in a 1.0°

radius around N 157B centred on the pointing direction within an energy interval of 100 GeV to 100 TeV. Of the previous 56438 gamma ray events, 8849 were filtered out, mostly by the radial cuts.

The sky map in Figure 7.7 displays the selected gamma ray events within a 1.0° radius around N 157B. From Figure 7.7 it can be deduced that 30 Dor C is a much fainter source with a right ascension off-set from that of N 157B by a few tenths of a degree. It appears that 30 Dor C is slightly brighter than the present background and is, thus, subject to contamination from not only N 157B but from background events as well. N 157B is also subject to contamination from background events.

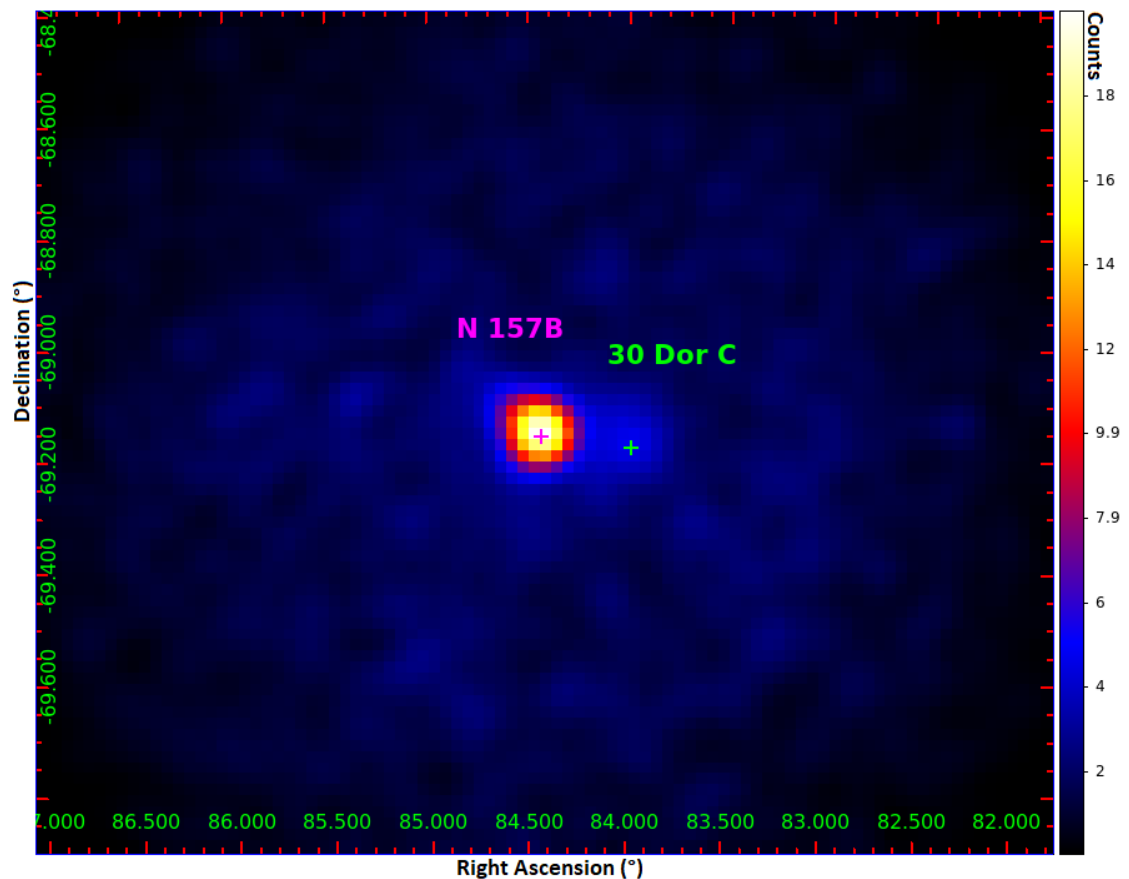


Figure 7.7: Sky Map of N 157B and 30 Dor C with no background subtraction. The sky map shown displays both N 157B and 30 Dor C in a 1° radius centred on N 157B. A gaussian smoothing kernel was applied with a standard deviation of 1.5 pixels. Areas on the perimeter of the sky map showing zero counts lie outside the 1.0° radius of events.

7.2 Morphological Analysis

This section aims to deduce the morphology of N 157B's fainter companion, 30 Dor C while simultaneously fitting the spatial position of N 157B. Two separate, nested morphological models were evaluated, which define 30 Dor C as a point source as well as a radial disk, respectively. More complex models consisting of more parameters were also evaluated, such as a radial shell model and an elliptical disk model.

The radial shell model failed to converge upon fitting since the inner radius to be probed is much smaller than the PSF. The elliptical disk model over-estimated the semi-minor radius to 0.5° as a result of fitting background sources in addition to 30 Dor C; thus, only a comparison of the point source model and the radial disk model is presented. It follows that this section investigates whether or not the addition of a radial component to the morphology of 30 Dor C provides a more accurate representation of its distribution of gamma ray events. While spectral parameters were also fitted, a detailed spectral analysis of both sources is performed later in Section 7.3.

7.2.1 Morphological Models Used

This section gives some insight into each of the two nested models used in determining the morphology of 30 Dor C and the position of N 157B. A description of the spatial component of each model is given. Across all test models, N 157B was assumed to be a point source with a power-law spectrum, of the form of Equation 6.2.2. , since there is no justification for additional spatial parameters for such a faint source. The spectrum of 30 Dor C was also assumed to follow the same power-law relation. The observation definition XML file containing the individual background models, that being a CTA IRF background, for each run within the observation list was taken as the background component in each of the model definition files for the two nested models.

7.2.1.1 Point Source Model

The first model to be fitted to the definition file of selected observations hypothesises that 30 Dor C has negligible spatial extent, making it possible to approximate its morphology to that of a point-like source. That is, it is described by only two spatial parameters, that being the right ascension and the declination. For convenience this point source model will be referred to as the initial model, H_0 . It follows that the overall spatial component $M_{spatial}(x, y)$ is described by a single spatial point, consisting of the right ascension and the declination of the source.

7.2.1.2 Radial Disk Model

This alternative model, H_1 , assumes that the morphology of 30 Dor C is represented by a radial disk. It follows that the spatial component, as defined in GammaLib and used by CTools, is of the form:

$$M_{spatial}(r, \theta) = A * M_{norm} \begin{cases} 1 & 0 \leq r \leq R_d \\ 0 & otherwise \end{cases}$$

where r is the angular separation between the disk centre and the observation point of interest and A is the amplitude. M_{norm} is the normalisation constant defined as $\frac{1}{2\pi(1-\cos(R_d))}$ and has units of sr^{-1} . In the case where $R_d \ll 2\pi$, M_{norm} may be reduced such that the previous Equation may be approximated as:

$$M_{spatial}(r, \theta) = \frac{A}{\pi R_d^2} \begin{cases} 1 & 0 \leq r \leq R_d \\ 0 & otherwise \end{cases} \quad (7.2.1)$$

where $r = \sqrt{x^2 + y^2}$

The radial extent of the disk defined within the model definition file is represented by R_d . The distance from the disk origin is defined as r and x and y are the true angle along the right-ascension and declination axes, respectively. Essentially, one may interpret Equation 7.2.1 to assume 30 Dor C to have a symmetric spatial extent

with an intensity that is uniformly distributed over a given radius. Unlike H_0 , the radial disk model requires an additional spatial parameter to the right ascension and the declination of a source, that being the radius of the source.

7.2.2 Methodology

The approach used in assessing the morphology of 30 Dor C requires the model definition files of each of the two test models, that is H_0 and H_1 , to be fitted to the event lists of selected runs. As before, this is completed by performing a maximum likelihood fit of each model to the data. All spatial and spectral properties of the test models were fitted with the exception of the pivot energy.

The log-likelihoods associated with each of the fitted models were determined and compared. Since H_0 has fewer parameters, the associated likelihood value will be less than that of the alternative model, H_1 . As per Chapter 5, in order to determine if the improvement of the alternative likelihood value over the null value is significant, the associated p-value needs to be determined.

Thus, the fits of the two models were assessed by calculating the significance and p-value associated with the difference between the log-likelihoods of each model. The large size of the data set and the fact that the parameters of the point source model are a subset of the radial disk model make it possible to invoke Wilks theorem[48] to determine the p-values. As before, a lower p-value suggests strong evidence that of the two models being compared, the parameter-rich model is a better representation of the observed data. The significance level of 5.3σ defined in Chapter 5 was taken as the threshold value which corresponds to a p-value of 10^{-7} . Thus, if the p-value of two models being compared lies below the threshold of 10^{-7} there is reason to assume that the parameter-rich model, H_1 , is better in describing the observed data. This implies that if the significance of the two models under comparison is greater than 5.3σ , it is likely that the parameter-rich model is a better fit to the observed data set.

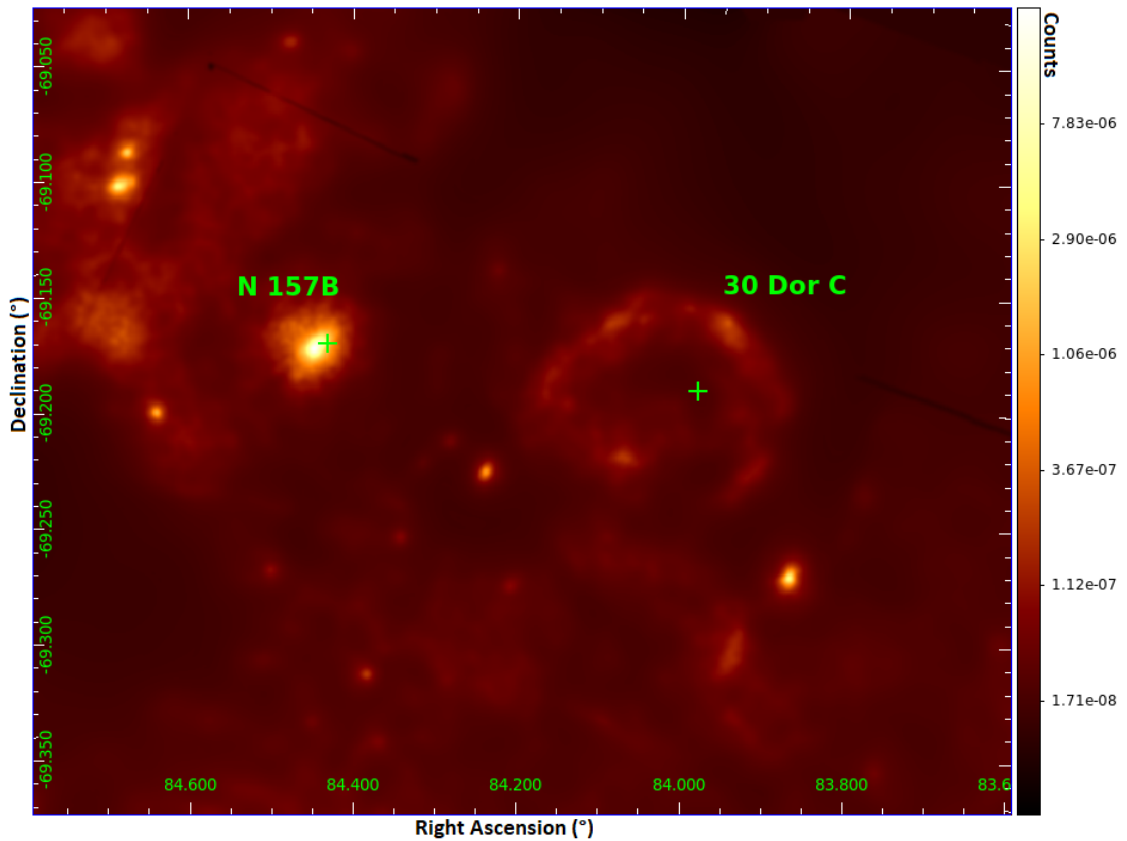


Figure 7.8: XMM-Newton X-ray Flux Image. The image was supplied by the H.E.S.S. collaboration[13] in FITS format.

Only if the p-values support the alternative model over the null model, were the best-fit parameter values of the alternative model further analysed to determine if the parameters converged on a reasonable value. This analysis included analysing the best-fit spatial parameter values with the associated errors and superimposing these values on the sky map in Figure 7.7. Thereafter, the same best-fit spatial parameters were superimposed on an x-ray image of the two sources, shown in Figure 7.8, in order to compare the source morphologies to that in a different energy regime. The difference, ΔN , between the number of observed gamma ray events and the number of gamma ray events predicted by each model was determined upon fitting. It is apparent that a large difference would suggest that the fitted model either did not account for a gamma ray source in the field of view or over sampled a source, thus, making it a poor representation of the observed data.

A spatial residual inspection was also performed of each fitted model by means

of generating residual maps. Areas on the map where extreme over sampling or under sampling is present suggest that the fitted model defines a source not present in the observed data or fails to define a source that is present respectively.

Spectral information of both N 157B and 30 Dor C was also considered in this analysis step and was obtained using the specifications described in Chapter 4 regarding *csspec*. While spectral information is looked at, at this stage, an in-depth spectral analysis will only be performed in Section 7.3. Spectral information looked at in the present section serves as a complement to the morphology results.

7.2.3 Results

The current section looks at the difference in likelihood values between the null and the alternative models as well as the significance associated with this difference. In the case that the p-values support the alternative model, the best-fit parameter values were analysed. Thereafter, the model which best describes the morphology of 30 Dor C and position of N 157B given the observed data set was identified.

7.2.3.1 Likelihood, P-Value and Significance Comparison

The fit results of each model, that is the log-likelihood values, the difference between the observed and predicted gamma ray events for 30 Dor C and N 157B are displayed in Table 7.4.

Table 7.4: Log-Likelihood Values and Event Residuals for 30 Dor C Morphology Analysis

Model	Maximised Log-Likelihood	Predicted Events (N_{pred})	$\Delta N = N_{obs} - N_{pred}$
H ₀	-112316.7	8854.4	-5.5
H ₁	-112300.4	8849.1	-0.07

As established in Chapter 5, the parameter-rich model, being H₁ in this case,

would yield a higher log-likelihood value even if it were not a better representation of the data due to the additional spatial parameters defined in the model. The p-value associated with the difference in likelihoods of the two models is needed to conclude if this increase is significant or not.

Table 7.5 shows the p-value obtained when comparing the log-likelihoods of the null and alternative model along with the associated significance for 30 Dor C. Considering the threshold p-value of 10^{-7} , with an associated significance of 5.3σ , the p-value presented in table 7.5 lies one order of magnitude below this threshold p-value. This suggests that the alternative model, H_1 , which assumes a radial disk-like morphology for 30 Dor C, is a more realistic representation of the observed data set than the null model H_0 .

Table 7.5: P-Values and Associated Significance for 30 Dor C Morphology Analysis

Models Compared	P-Value	Significance
H_0 & H_1	1.1×10^{-8}	5.7

This finding suggests reasonable cause to reject the point source model, H_0 , as a possible morphology of 30 Dor C and to accept the radial disk model, H_1 , as the most appropriate morphology of 30 Dor C in the TeV regime.

7.2.3.2 Best Fit Parameter Values of 30 Dor C and N 157B

The present section evaluates the best-fit parameter values obtained after performing a maximum likelihood fit and p-value analysis of the two test models, with the knowledge that the p-values support the alternative model.

The best-fit results of 30 Dor C and N 157B displayed in Tables 7.6 and 7.7, respectively, coincide with the spatial and spectral properties of both sources determined by the H.E.S.S. Collaboration[13] referred to in Chapter 2. The errors associated with the fitted parameters are all 1 to 3 orders of magnitude smaller than

that of the parameter values themselves, indicating low variance in the fitted values. The only significant deviation from the published data presented in Chapter 2 is observed in the fitted differential flux of 30 Dor C of the radial disk model. Even though the spectral properties are fitted and presented in the current section, an in-depth analysis and discussion is only performed in 7.3. The present section gives focus to the spatial properties of the two sources.

Table 7.6: Best Fit Parameter Values of 30 Dor C. Note that the pivot energy is not fitted, hence the associated error is not applicable. The pivot energy value is presented simply for convenience.

Model Parameters	Point Source Model (H_0)		Radial Disk Model (H_1)	
	Best Fit Values	Errors	Best Fit Value	Errors
Prefactor ($\text{ph.cm}^{-2}.\text{s}^{-1}.\text{MeV}^{-1} \times 10^{-19}$)	2.06	± 0.40	3.09	± 0.54
Spectral Index	-2.52	± 0.18	-2.52	± 0.15
Pivot Energy (MeV)	10^6	N/A	10^6	N/A
Right Ascension ($^\circ$)	83.97	± 0.01	84.0	± 0.02
Declination ($^\circ$)	-69.17	± 0.01	-69.17	± 0.007
Radius ($^\circ$)	N/A	N/A	0.08	± 0.009

Table 7.7: Best Fit Parameter Values of N 157B for each spatial model. Note that the pivot energy is not fitted, hence the associated error is not applicable. The pivot energy value is presented simply for convenience.

Model Parameters	Point Source Model (H_0)		Radial Disk Model (H_1)	
	Best Fit Values	Errors	Best Fit Value	Errors
Prefactor ($\text{ph.cm}^{-2}.\text{s}^{-1}.\text{MeV}^{-1} \times 10^{-18}$)	1.15	± 0.08	1.13	± 0.08
Spectral Index	-2.68	± 0.07	-2.69	± 0.07
Pivot Energy (MeV)	10^6	N/A	10^6	N/A
Right Ascension ($^\circ$)	84.45	± 0.01	84.45	± 0.01
Declination ($^\circ$)	-69.16	± 0.002	-69.16	± 0.002

The point source model, H_0 , predicts a differential flux of $2.06 \pm 0.40 \times 10^{-19}$ $\text{ph.cm}^{-2}.\text{s}^{-1}.\text{MeV}^{-1}$ while the radial disk model, H_1 , predicts $3.09 \pm 0.54 \times 10^{-19}$ $\text{ph.cm}^{-2}.\text{s}^{-1}.\text{MeV}^{-1}$ for 30 Dor C. It was found that the differential flux fitted by H_0

lies within approximately 1 standard deviation and that fitted by H_1 within approximately 3 standard deviations from that obtained by the H.E.S.S. collaboration, $1.6 \pm 0.04 \times 10^{-19} \text{ ph.cm}^{-2}.\text{s}^{-1}.\text{MeV}^{-1}$.

The number of standard deviations of the differential flux predicted by H_0 from that of H.E.S.S. produces a p-value of 0.21. Up to a significance of level of 0.01 the difference in the results is not statistically significant. In terms of H_1 , a p-value of 0.003 was produced, meaning that the difference is significant up to a significance level of 0.01.

As established, the data does support a circular morphology for 30 Dor C. Thus, if a radial disk-like shape is assumed for the emission of 30 Dor C then a point-like morphology will not be sufficient in describing the gamma ray emission of 30 Dor C. A point-like morphology will only account for the central emission and neglect the emission further out. This explains why a greater differential flux is predicted by the radial disk model.

Figure 7.9 shows the spectral points of 30 Dor C produced by CTools superimposed on those determined by the H.E.S.S collaboration [13]. The spectral generation method made available by CTools, which makes use of ten logarithmically-spaced energy bins, was used in the generation of the 30 Dor C spectrum. More details regarding spectrum generation is discussed in Section 7.3.

In both cases, the spectral shape is assumed to follow a power law while the morphology of 30 Dor C is represented as a point source by the H.E.S.S. Collaboration and a radial disk for the CTools analysis. A slight upward shift in the spectrum determined using CTools is observed from that published by the H.E.S.S. Collaboration which corresponds to the greater differential flux (prefactor) predicted by CTools. While this deviation between these spectral points of the two data sets exists, the deviation is still consistent with the associated errors. Thus, even though a 2 standard deviation difference in differential flux is realised, the data is still in

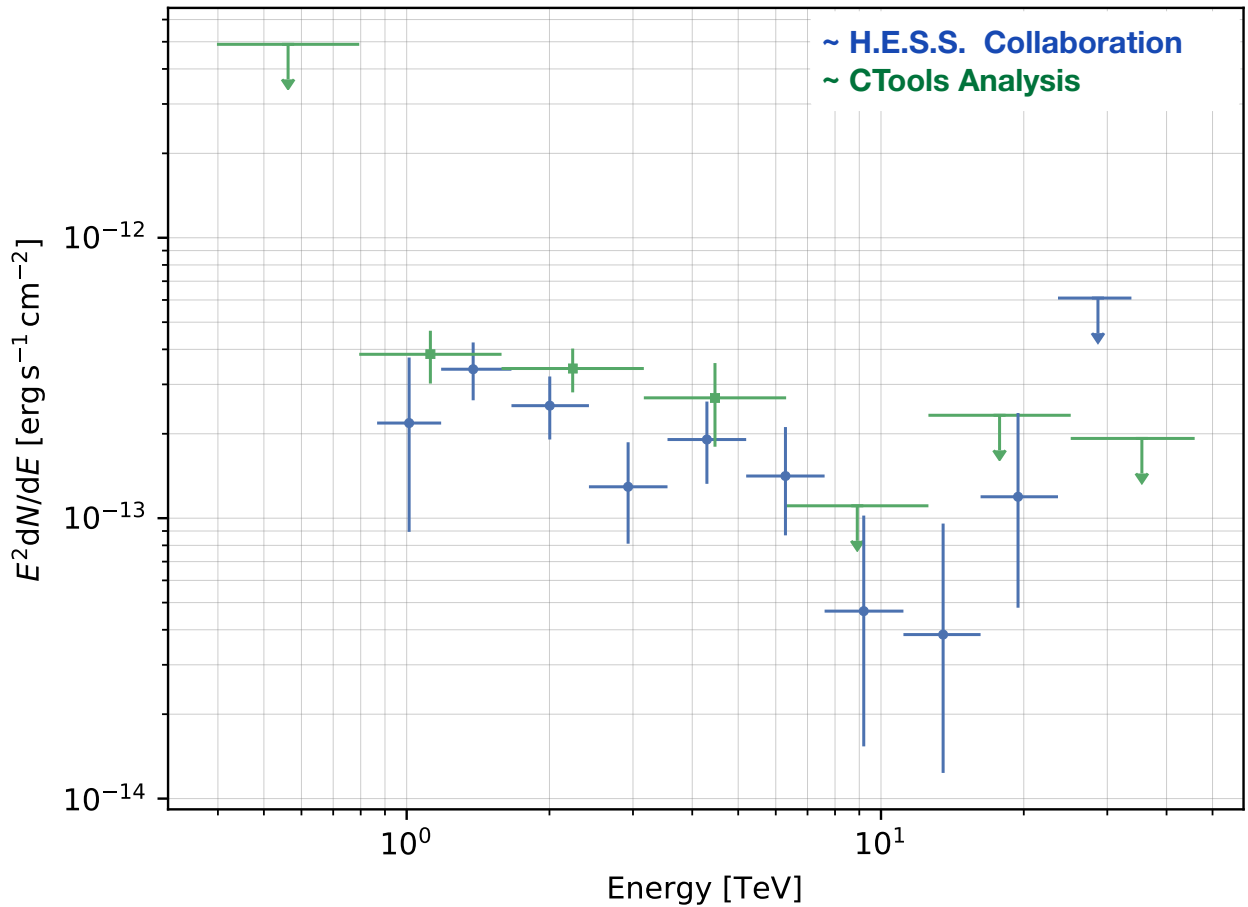


Figure 7.9: 30 Dor C spectrum superimposed on the H.E.S.S. Collaboration spectrum. The log-log plot shows the spectrum as determined by CTools (green) overlaid on the spectrum as determined by the H.E.S.S. Collaboration[13] (blue) of 30 Dor C with the associated error bars and upper flux limits.

agreement with that published by H.E.S.S.

The spectral index fitted by both the null and alternative models for 30 Dor C fall within approximately 0.3 standard deviations from the H.E.S.S. results. These deviations produce a p-value of 0.01 which is not statistically significant up to a significance level of 0.01. The same is observed for the spectral index fitted by both test models for N 157B. The values fitted by both models fall within 1 standard deviation of that determined by the H.E.S.S. Collaboration meaning that the differ-

ence observed is not significant.

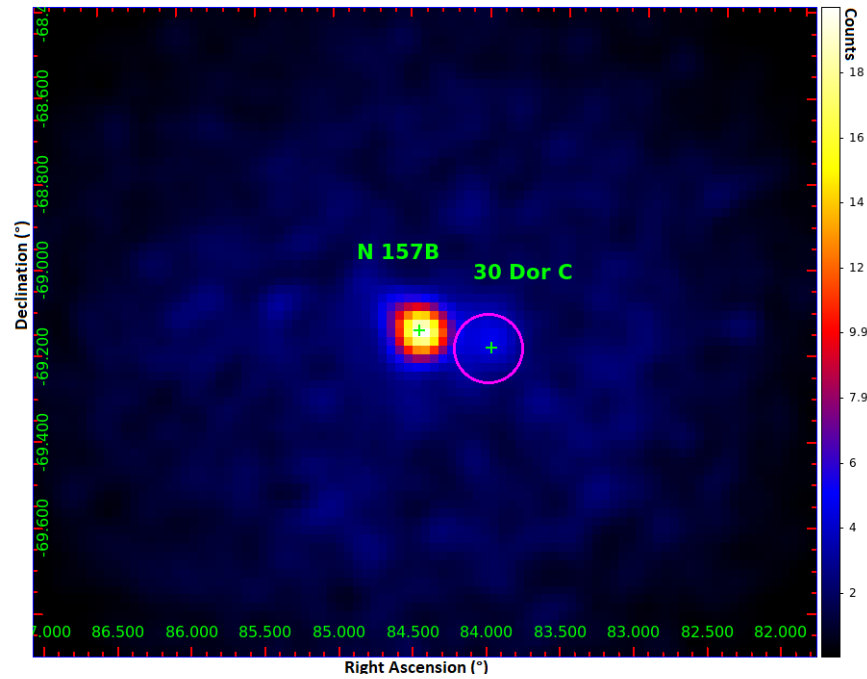
Figure 7.10 displays the morphology fit results of both test models, H_0 and H_1 , superimposed on sky maps of N 157B and 30 Dor C. The sky map shown in Figure 7.10a indicates that the best-fit spatial parameters agree with the distribution of gamma-ray events of 30 Dor C. The same may be said for Figure 7.10b which shows the best fit morphology of both models superimposed on an X-ray image of 30 Dor C and N 157B in the energy range 0.5 keV to 8 keV. The position of N 157B also seems to coincide with the location of the associated gamma ray events on the sky map.

The morphologies of both the null and the alternative model do appear to be slightly off-set in the X-ray image for 30 Dor C. In the case of an extended source the various structural properties, revealed in different energy regimes, would change the average position of the source. This observation is in agreement with the fact that the data supports the alternative model. There is also an offset present in the position of N 157B in the X-ray image; however, given the symmetric errors in the right ascension and declination along with the little variance in the fitted parameters as well as the fit statistics, the source position may be accepted.

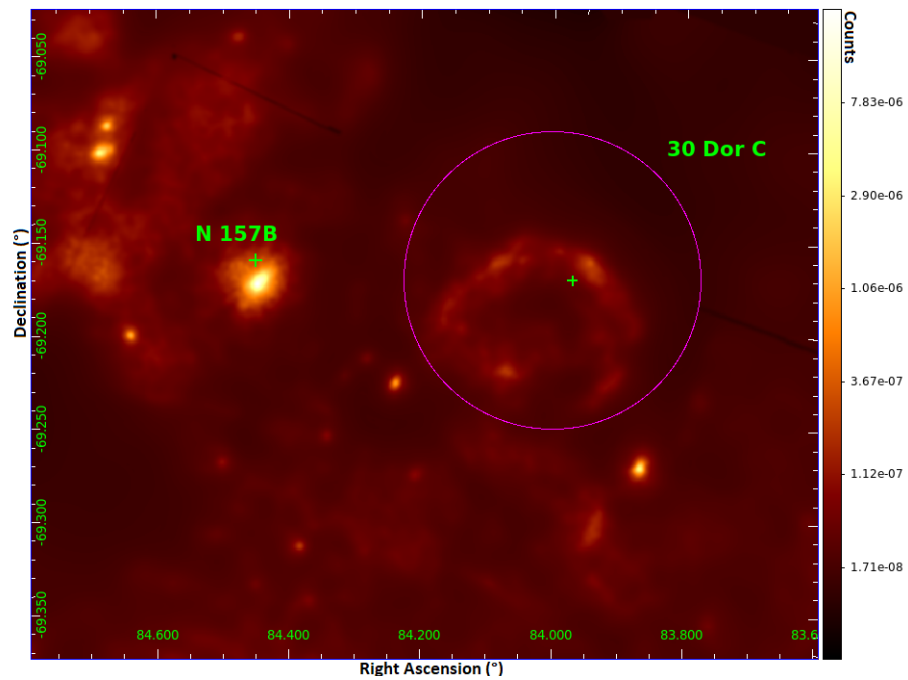
Ultimately, there is no immediate visual indication that the best-fit spatial parameter values produced neither unrealistic morphologies for 30 Dor C nor unreasonable positions for N 157B for both test models.

The best-fit parameter values for N 157B are approximately identical across both H_0 and H_1 which is to be expected since the model component describing N 157B in both H_0 and H_1 is the same with the deviations being attributed to the different shapes and flux of 30 Dor C across the two test models which would affect the background contaminating the N 157B flux.

With the best-fit parameters of both models validated and analysed, it is safe to



(a)



(b)

Figure 7.10: Morphology of Test Models Superimposed on Sky Maps. (a) The best-fit morphology of H_0 and H_1 overlaid on a sky map of gamma ray events. (b) The XMM-Newton x-ray flux image supplied by the H.E.S.S. collaboration[13] depicting a 0.2° field of view surrounding N 157B and 30 Dor C with the best-fit morphology overlaid. A logarithmic scale was applied to (b). A gaussian smoothing kernel was applied to both (a) and (b) with a standard deviation of 1.5 pixels (0.003°). Green crosses represent the null model while the magenta circles and crosses represent the alternative model. More structural properties of 30 Dor C is revealed in (b).

October 30, 2020

assume that a circular morphology is the most appropriate morphology for 30 Dor C, as supported by the p-values. As a sanity check, the spatial residuals of both models will also be compared, in the proceeding section, in order to further confirm the acceptance of a radial disk morphology for 30 Dor C.

7.2.3.3 Spatial Residual Inspection

Figures 7.11a and 7.11b display the spatial residuals of 30 Dor C with N 157B also present, respectively. Comparing the two residuals it is apparent that there is a reduction in the under-sampling within the vicinity of 30 Dor C for the radial disk model, making the overall map more uniform.

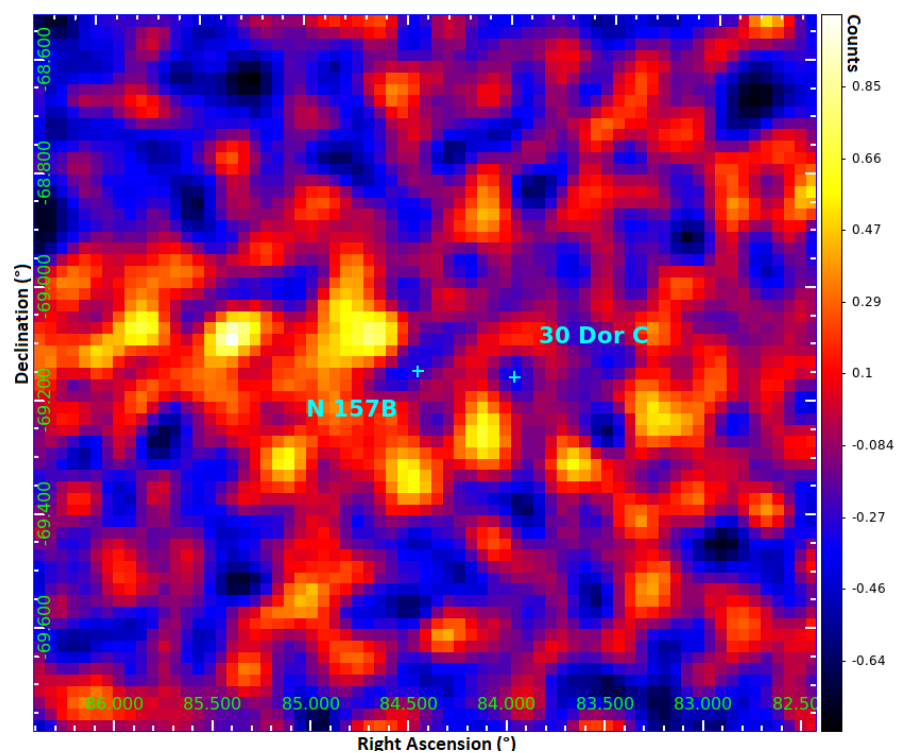
The fact that the radial disk model does offer some improvement in the overall spatial residual of the observed data set further motivates the acceptance of a radial disk morphology for 30 Dor C.

7.2.4 Conclusion

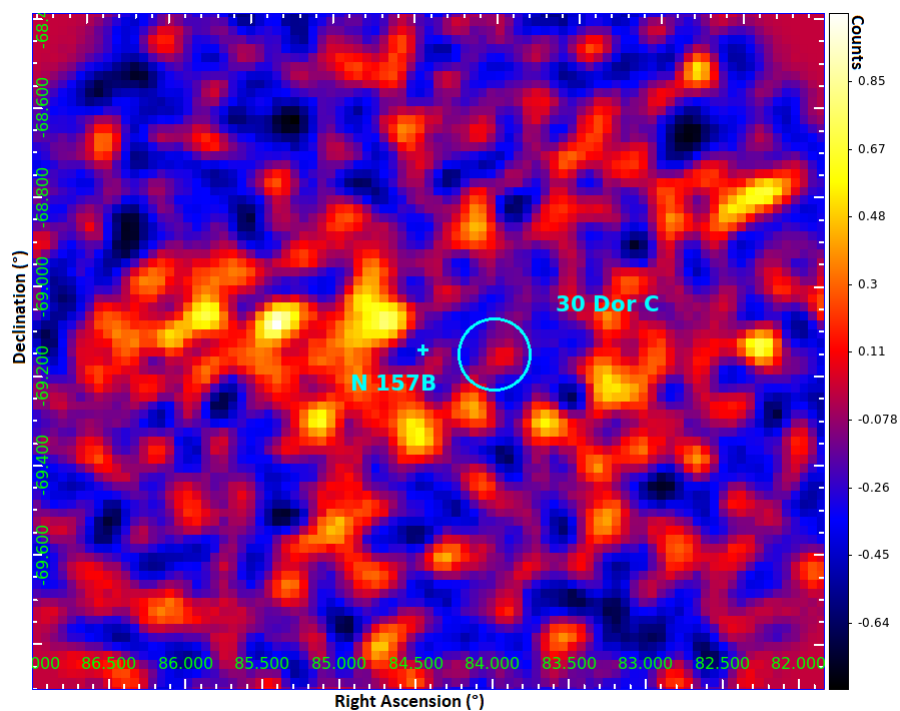
From the preceding sections it may be concluded that the morphology of 30 Dor C and the spatial position of N 157B was successfully determined. It was deduced that a radial disk-like morphology was a suitable representation 30 Dor C, producing a spatial model component, in units of sr^{-1} , of the following form:

$$M_{\text{spatial}}(r, \theta) = \frac{A}{\pi \times (0.08 \pm 0.009)^2} \begin{cases} 1 & 0 \leq r \leq 0.08 \pm 0.009 \\ 0 & \textit{otherwise} \end{cases} \quad (7.2.2)$$

It has been assumed that 30 Dor C has a symmetric spatial extent with a gamma ray intensity that is uniformly distributed over a radius of $0.08^\circ \pm 0.009^\circ$, which is intuitive given the superbubble like nature of 30 Dor C, and is visually supported by the sky maps in Figure 7.10a.



(a)



(b)

Figure 7.11: Spatial residual maps of 30 Dor C. The significance algorithm was used in order to determine the residuals. A gaussian kernel was also applied with a standard deviation of 1.5 pixels to smooth the data.

30 Dor C was found to have a right ascension of $84.0^\circ \pm 0.02^\circ$ and a declination of $-69.17^\circ \pm 0.01^\circ$. Additionally, the right ascension and declination of N 157B was found to be $84.45^\circ \pm 0.01^\circ$ and $-69.16^\circ \pm 0.002^\circ$, respectively, also with a significance level of 5.3σ . All uncertainties associated with the best-fit spatial parameters of both 30 Dor C and N 157B are 2 to 3 orders of magnitude smaller than the actual best-fit values, allowing one to place confidence in the precision of the best-fit results.

Ultimately, CTools was successfully used to determine the morphology of 30 Dor C while fitting the position of N 157B. That is, the analysis was able to successfully distinguish two sources with an offset of 0.15° where source contamination is a factor and one source is outshined by its companion.

Given that the morphology of 30 Dor C and the position of N 157B have been determined, the next methodical step would be to evaluate various spectral models in an attempt to determine the spectral energy distribution of N 157B and 30 Dor C, which is carried out in the subsequent sections.

7.3 Spectral Analysis

This section aims to determine the spectral energy distribution of N 157B while simultaneously fitting the spectrum of 30 Dor C. As per the morphological analysis, various spectral models were considered, namely one in which the spectrum of N 157B is described by a power law and two alternative models where the spectrum is described by an exponentially cut-off power law and a log parabola spectrum, respectively. Thus, this section investigates if the addition of a cut-off or a curvature in the spectrum of N 157B will result in a more accurate spectral energy distribution of gamma ray events. All models converged upon fitting and the results are presented in the following sections. The background model, that being the CTA IRF background, used in the previous section was implemented.

We found that the data of N 157B does not support anything more complex than a power law, at least within the H.E.S.S. energy range between 0.1 TeV and 100 TeV. If a cut-off in the spectrum does exist, then it would lie either below or above the H.E.S.S. energy range. It is possible to test for a lower energy cut-off by means of utilizing Fermi-LAT data. It follows that lower energy gamma-ray data of N 157B from Fermi-LAT was combined with the spectrum predicted by CTools such that the existence of a lower energy cut-off may be tested.

We obtained the Fermi-LAT data from the LAT collaboration[14] and analysed the 6 years worth of data of gamma-ray emitters in the LMC in the 0.2 GeV - 100 GeV range. We established that N 157B is a point-like source with a spectrum observed with a spectral index of -2.68 ± 0.07 in the 0.5 GeV to 100 GeV range.

As established in Chapter 2, N 157B is accompanied by photon fields from surrounding structures which contribute to its brightness by means of inverse Compton emission[18]. To further probe the fundamental particle acceleration and evolution processes of N 157B, these photon fields were taken into account when testing for a lower energy cut-off.

That is, an attempt was made to produce a fitted model explaining not only the non-thermal features of N 157B, but a model which also describes the complete spectral distribution of gamma rays of N 157B. These non-thermal features include the inverse Compton emission as a result of the upscattering of electrons off the warm and cold photon fields of LH 99, the cosmic microwave background and the 30 Doradus nebula.

As mentioned in Chapter 2, the H.E.S.S. Collaboration [18] has made an attempt to study the spectral distribution of N 157B as well as its non-thermal features by means of a multi-wavelength leptonic model. They assume a cooling break is present in the spectrum of N 157B and proceed to measure the magnetic field and total electron energy, ultimately making an assumption on the age of N 157B. The spectral

index quoted in the paper was assumed from a high-energy cooling break of 1.1 TeV to be -2.60. The total electron energy, W_e was assumed to be 4×10^{49} erg.

We now assume the electron population to be a power law with a spectral break. The break was modeled as an exponential cut-off as it is the simplest form of a spectral break, having only one additional spectral parameter over a power law. No assumption was made on the nature of the spectral break in the sense that it could indicate the maximum acceleration energy of the electrons or a cooling break as discussed by the H.E.S.S. Collaboration[18]. The minimal energy of the electrons was fixed to 54 GeV, which is the intrinsic break assumed by the H.E.S.S. Collaboration[18].

Now, we fit the spectrum to the combined H.E.S.S. and Fermi data for the first time. We assume a functional form of Equation 6.2.1 for the electron spectrum but leave the spectral break as a free parameter to be fitted.

7.3.1 Spectral Models Used

The present section describes the particulars of the spectral components of the two spectral models used. In Section 7.2, we determined that the morphology of 30 Dor C is best represented by a radial disk-like source. It follows that for the subsequent sections, 30 Dor C will be assumed to have a radial disk-like morphology for all test models. The assumption that the spectrum of 30 Dor C follows a power law, the form of Equation 6.2.2, is preserved. The morphology of N 157B is assumed to be point-like. As in section 7.2, the observation definition file consisting of the individual background models was taken as the background component for both of the spectral models evaluated.

7.3.1.1 Power Law Model

The first spectral model to be fitted to the observed data set assumes the spectrum of N 157B to follow a power law. Thus, the spectral model component is a power law

function of the form of Equation 6.2.2. That is to say, the spectral intensity of the gamma-ray source experiences a proportional relative change through the emission energy range of the source. As seen in Equation 6.2.2, the spectral component of this power-law model is described by three parameters, namely the pivot energy, prefactor and the spectral index of the source. As per Section 7.2, this power-law model will be termed the null model, H_0 , for the purpose of this stage of the analysis.

7.3.1.2 Exponentially Cut-Off Power Law Model

The exponentially cut-off power-law model assumes that the spectrum of N 157B coincides with a power law for a portion of the observed TeV energy range after which the spectrum deviates and experiences an exponential decay. Beyond the cutoff energy, the spectral intensity falls off exponentially. It follows that the spectral component of this alternative model is described by an exponentially cut-off power law, of the form of Equation 6.2.1. This model will serve as the alternative model H_1 for this stage of the analysis. The spectral component of the alternative model consists of an additional parameter compared to that of H_0 representing the cut-off energy.

7.3.1.3 Log Parabola Model

The final alternative model considered assumes that the spectrum of N 157B may be described by a curved power law, a log parabola function of the form of Equation 7.3.3.

$$\frac{dN}{dE}(E) = k_o \left(\frac{E}{E_o} \right)^{\gamma + \eta \ln\left(\frac{E}{E_o}\right)} \quad (7.3.3)$$

Equation 7.3.3 contains an additional term in the exponent, when compared to the pure power law given by Equation 6.2.2, which gives the spectrum its characteristic curve. The curvature constant η defines the degree of curvature of the power law. As per convention this alternative model will be referred to as model H_2 .

7.3.2 Methodology

7.3.2.1 Model Fitting

As per the morphological analysis in Section 7.2, all test models, H_0 , H_1 and H_2 are required to be fitted to the observation definition file of the selected runs described in Section 7.1. All spatial parameters of both 30 Dor C and N 157B were fixed. Thus, only spectral parameters were fitted, with the exception of the pivot energy, to the observed data by means of a maximum likelihood fit. The spatial parameters were fixed to the best fit values obtained in Section 7.2.

We analysed the best-fit spectral parameters obtained after performing a maximum likelihood fit for each test model and used these parameters to determine the spectral energy distribution of N 157B predicted by each model. A binning of 10 logarithmically spaced energy bins were implemented for the spectrum generation where the best-fit source flux as well as the associated errors, flux limits and predicted events were determined for each energy bin for each test model. Only the bins for which the flux produced a test statistic greater than 9 and is greater than the flux error were taken as spectral points.

7.3.2.2 Fit Analysis

As before, the log-likelihood values obtained after fitting both the null and the alternative models to the observed data set were compared. In this case both the exponentially cut-off power law model, H_1 , and the log parabola model, H_2 , are considered as the parameter rich models, due to the additional cut-off variable and curvature parameter, respectively. It follows that H_1 and H_2 would produce the greater log-likelihood value, due to the additional parameters, indicating an improvement in the fit. If this improvement is not significant then fitting the alternative model to the observed data failed and the null model is accepted. This would indicate that if a curvature in the spectrum does exist, the data are not sensitive enough in to detect it. If this is not the case and the improvement is significant then the converse is true.

Again the p-value and the significance obtained when comparing the log-likelihood values were analysed and used to further discriminate the model which provides the better spectral description of N 157B. Both the alternative models are nested models of the null model but not each other, therefore, p-value and significance calculations were only performed between each alternative model and the null model and not between the alternative models themselves. It follows that the model which shows the greatest increase in the log-likelihood value when compared to that of the null model is more likely to be a true representation of the data.

As per section 7.2, the threshold of 5.3σ was implemented. A p-value below 10^{-7} indicates that the spectrum of N 157B favours that described by the alternative model being compared and the power law model is rejected. If the p-value lies above the threshold the converse is true. It follows that if the significance is greater than 5.3σ , it is likely that the respective alternative model is a better fit to the observed data set. The alternative model which offers the greater significance, lower p-value, will be favoured, provided that the respective p-value and significance lie below the threshold values. Note that the p-value threshold will occur at different values of the test statistic for the two alternative models due to the differing number of degrees of free parameters.

An inspection of the spectral residuals were also performed. Intuitively, the model which produces a residual which is randomly distributed and in which no large-scale shapes are present is the model which provides a better representation of the data.

7.3.2.3 Non-Thermal Spectral Features

After using CTools to determine a spectrum for N 157B, we produced a combined spectrum with Fermi-LAT data and made an attempt to fit the non-thermal emission from the relativistic electron populations while searching for a lower energy cutoff;

that is, the inverse Compton scattering off the warm and cold photon fields of the star cluster LH 99 and the cosmic microwave background and the 30 Doradus nebula.

The electron particle distribution was taken to assume an exponentially cut-off power law, in the energy range 54 GeV to 100 TeV, which is defined explicitly in Equation 7.3.4 where A is the amplitude of the spectrum in units of particles.eV⁻¹.

$$f(E) = A \left(\frac{E}{E_0} \right)^\gamma \exp \left(\frac{-E}{E_{cut}} \right) \quad (7.3.4)$$

No assumptions were made on the nature of the spectral break in the sense that it could indicate the maximum acceleration energy of the electrons or could be due to a cooling break or other mechanisms. The intrinsic break of 54 GeV in the electron spectrum was taken as the lower limit of the energy range being analysed.

The photon fields were assumed to be blackbody emitters with temperature and energy densities given in Table 2.1. The energy densities of the hot and cold dust of LH 99 is greater than that of the neighbouring photon fields since N 157B is thought to be located in or behind LH 99.

Inverse Compton emission is assumed to be the main production channel of the gamma-rays; thus, an inverse Compton radiative model was chosen to represent the non-thermal emission from N 157B. Both the radiative model and the particle distribution model were fitted to the combined Fermi-LAT and H.E.S.S. flux points, including upper limits, in the energy range of 0.01 TeV to 100 TeV. More specifically, a spectral model which convolves an exponentially cutoff power law electron spectrum with an inverse Compton radiative model was produced and fitted to the combined spectrum.

Table 7.8 describes which model parameters were fixed prior to fitting and which were left as free parameters to be fitted to the combined spectrum. The photon field energy densities and temperatures used for the various photon fields were taken from

Table 2.1. The pivot energy for the electron spectrum was fixed at 1 TeV and the distance to the source was set to 50 kpc. The total electron energy W_e is a derived value from the integral over the spectral model.

Table 7.8: Non-Thermal Spectral Model Parameters

Model Parameters	Free or Fixed
Spectral Index α	Free
Cutoff Energy E_c (TeV)	Free
Amplitude (particles.eV ⁻¹)	Free
Pivot Energy (TeV)	Fixed
Photon Field Energy Density (eV.cm ⁻³)	Fixed
Photon Field Temperature (K)	Fixed
Distance (kpc)	Fixed

The astropy package [Naima](#)[52] was used for all work regarding the determination of non-thermal properties. The photon energy densities and temperatures, electron particle distribution and source distance were taken as input parameters for the inverse Compton radiative model while the remainder of the parameters formed part of the spectral model describing the electron particle distribution. Naima uses MCMC sampling of the model parameter likelihood distributions in order to determine the best-fit parameter values. The fitted results were compared with those of the the H.E.S.S. collaboration[18] and plotted over the combined spectrum.

7.3.3 Results

The current section presents the best-fit spectral parameters of both N 157B and 30 Dor C for all three spectral test models considered with the associated uncertainties. Statistics, such as log-likelihood values, p-values and significance used to compare the goodness of the fit of each model to the data is also presented. It was found that the observed data did not support a spectrum more complex than a power law for N 157B.

7.3.3.1 Likelihood, P-Value and Significance Comparison

Table 7.9 contains the log-likelihood values associated with each fitted test model. It is apparent that there is an improvement in the fit across both alternative models, since there is an increase in the log-likelihood values when compared to that of the null model; however, this is expected due to the additional spectral parameters in both alternative models. While there is an improvement in the fits of both models H_1 and H_2 , the p-values would have to be analysed to determine if the difference in likelihoods is significant or not.

Table 7.9: Log-Likelihood Values and Event Residuals for N 157B Spectral Analysis

Model	Maximised Log-Likelihood	Predicted Events (N_{pred})	$\Delta N = N_{obs} - N_{pred}$
H_0	-112300.4	8854.4	-6.8
H_1	-112299.6	8849.1	-0.07
H_2	-112299.5	8849.1	-0.07

Applying the p-value threshold of 10^{-7} , 5.3σ , Table 7.10 reveals that both alternative models do not meet the threshold criteria. The p-value associated with the probability of the exponentially cut-off power law model being a better description of the spectrum of N 157B is 0.21 while that of the log parabola model is 0.18, neither of which offer a statistically significant improvement over the power law. Thus, it is apparent that neither the exponentially cut-off power law model nor the log parabola model offer a sufficient improvement in describing the data, such that a model more complex than a power law is not supported by the data and thus both alternative models may be rejected and the null model may be accepted.

Table 7.10: P-Values and Associated Significance for N 157B Spectral Analysis

Models Compared	P-Value	Significance
H_0 & H_1	0.21	1.26
H_0 & H_2	0.18	1.34

7.3.3.2 Best-Fit Spectral Parameter Values

The best-fit spectral parameter values obtained after performing a maximum likelihood fit of each of the spectral models to the observed data of N 157B and 30 Dor C is displayed in Tables 7.11 and 7.12, respectively. Since the null hypothesis is the only model justified by the p-values, only the best-fit parameters of the power law model are analysed.

Table 7.11: Best Fit Spectral Parameter Values of N 157B. Note that the pivot energy is not fitted, hence the associated error is not applicable. The pivot energy value is presented simply for convenience.

Model Parameters	Power Law Model (H_0)	
	Best-Fit Value	Errors
Prefactor ($\text{ph.cm}^{-2}.\text{s}^{-1}.\text{MeV}^{-1} \times 10^{-18}$)	1.14	± 0.08
Spectral Index	-2.68	± 0.07
Pivot Energy (MeV)	10^6	N/A

Table 7.12: Best Fit Spectral Parameter Values of 30 Dor C. Note that the pivot energy is not fitted, hence the associated error is not applicable. The pivot energy value is presented simply for convenience.

Model Parameters	power law Model (H_0)	
	Best Fit Value	Error
Prefactor ($\text{ph.cm}^{-2}.\text{s}^{-1}.\text{MeV}^{-1} \times 10^{-19}$)	3.09	± 0.51
Spectral Index	-2.57	± 0.15
Pivot Energy (MeV)	10^6	N/A

The best-fit differential flux of N 157B, that being the prefactor, fitted by H_0 falls within 1.2 standard deviations from the value obtained by the H.E.S.S. Collaboration, that is $1.3 \pm 0.1 \times 10^{-18} \text{ph.cm}^{-2}.\text{s}^{-1}.\text{MeV}^{-1}$ [13]. The p-value associated with this difference is 0.15; thus, this difference is not significant up to a significance level of 0.01. The power law model, H_0 , produced a best-fit spectral index of -2.68

for N 157B with an associated error of 0.07, which falls within 1 standard deviation of the spectral index, -2.8 ± 0.1 , obtained by the H.E.S.S. collaboration. This corresponds to a p-value of 0.16 which, as before, means that the difference in values is not significant up to a significance level of 0.01.

The best-fit spectral parameter values of 30 Dor C displayed in Table 7.12 appear to be similar to that fitted in the previous section. This is to be expected since the same power law spectral component was employed. The spectral index measured for 30 Dor C is within 1 standard deviation from that determined by the H.E.S.S. collaboration, -2.6 ± 0.2 , corresponding to a p-value of 0.45 which is not significant up to a significance level of 0.01. This suggests that the measurement is consistent with that of the H.E.S.S. Collaboration.

The differential flux fitted by the power law model for 30 Dor C lies within 3 standard deviations of that measured by the H.E.S.S. Collaboration, that being $1.6 \pm 0.04 \times 10^{-18} \text{ph.cm}^{-2}.\text{s}^{-1}.\text{MeV}^{-1}$. As previously discussed, the difference is significant and is a result of the circular morphology assumed for 30 Dor C. The excess flux predicted for 30 Dor C could be a result of the presence of diffuse emission within the vicinity of 30 Dor C; however, since an excess differential flux is not observed for N 157B, this may be ruled out.

Additionally, the uncertainty in the best-fit values produced by the power law model for N 157B and 30 Dor C are two and one orders of magnitude less than the best-fit values themselves, respectively, once again placing confidence in the precision of the fitted values.

7.3.3.3 Non-Thermal Features of N 157B

We now infer the particle distribution and radiative model from the combined H.E.S.S. and Fermi-LAT flux points of N 157B to determine the contribution of each photon field to the inverse Compton emission. The contributions of the indi-

vidual photon fields to the total emission can be seen in Figure 7.12.

The spectral energy distribution is plotted in Figure 7.12. The flux points of N 157B in the H.E.S.S. energy range, determined by CTools, is shown in green while the lower energy Fermi-LAT data is shown in blue. The spectral energy distribution of the spectral model fitted using Naima is represented by the solid blue curve. This curve describes the electron spectrum convolved with the inverse Compton radiative model as a result of the various radiation fields. The remaining plots display the individual flux contributions of each of the radiation fields to the spectral energy distribution.

Since the area under the curve is the smallest compared to that of the other photon fields, it may be concluded that the cosmic microwave background is the smallest contributor to the inverse Compton emission of N 157B. This is to be expected since the cosmic microwave background energy density of 0.26 eV.cm^{-3} is low relative to that of the other photon sources, as seen in Table 2.1. This translates to fewer photons present acting as scattering surfaces for the population of relativistic electrons, hence, a minimal contribution to the inverse Compton emission.

The third largest to the inverse Compton emission of N 157B appears to be 30 Doradus followed by LH 99. Since N 157B is located in or behind the OB association LH 99, the density of LH 99 photons will be greater than that of 30 Doradus which is offset by 0.15° from N 157B. More specifically, as determined from Table 2.1, the energy density of 30 Doradus is approximately 5 times less dense than that of the LH 99 cold dust field and approximately half that of the warm dust. Thus the radiation field of LH 99 offers more photons for the electrons to scatter off of than that of 30 Dor C.

The cold dust emission of LH 99 is seen to be the dominant radiation field contributing to the inverse Compton emission of N 157B. The dense photon field, relative to the other photon field densities defined in Table 2.1, makes for the cold

dust of LH 99 to be the dominant contributor of the inverse Compton emission of N 157B. These trends are in agreement with that of the study performed by the H.E.S.S. Collaboration[18].

Table 7.13: Electron Population Parameters

Parameter	Value	Uncertainty (Lower Limit)	Uncertainty (Upper Limit)
Spectral Index α	-2.76	0.10	0.73
Cut-Off Energy E_c (TeV)	10.0	6.89	9.61
Total Electron Energy W_e (10^{49} erg)	1.06	0.54	0.22

The fitted parameters of the electron particle distribution, such as cut-off energy and spectral index, as well as the total energy content of the electrons, determined by integrating over the fitted model, are displayed in Table 7.13. The measured spectral index of $-2.76_{-0.10}^{+0.73}$ lies within 1 standard deviation from that of the spectral index of -2.6 determined by the H.E.S.S. Collaboration[18], corresponding to a p-value of 0.15. Thus the difference in values is not statistically significant up to a significance level of 0.01. It is noteworthy that this fitted result agrees to this extent with the spectral index inferred by the H.E.S.S. Collaboration[18] from an assumed cooling break.

The errors associated with the fitted spectral index are 1 one magnitude smaller than the fitted value which places some validity on the precision of the result.

The fitted cutoff energy of $10.0_{-6.89}^{+9.61}$ TeV differs by approximately 0.9 standard deviations from the H.E.S.S. value of 1.1 TeV. This difference corresponds to a p-value of 0.18 which is not significant up to a significance level of 0.01. The large associated error of the fitted value simply means more TeV measurements are needed in order to obtain a more precise measurement of the cutoff. The validity of the presence of a cutoff is not put into question since the actual existence of a break in the spectrum is already established by the H.E.S.S. Collaboration[18]. After the

cutoff within the spectrum, the spectrum will experience an exponential decay.

The total energy contained in the electrons was determined to be $1.06_{-0.54}^{+0.22} \times 10^{49}$ erg which is smaller than that hypothesised by the H.E.S.S. collaboration since the energy range over which the fit is done is smaller than that considered by the H.E.S.S. Collaboration[18].

Ultimately, this is the first time that the spectral energy distribution along with the non-thermal properties of N 157B are fitted using both H.E.S.S. and Fermi-LAT data. No assumptions were made regarding the mechanisms behind the break in the spectrum. It was only assumed that the break may be modeled as a cutoff in the spectrum. Given that different analysis methods were used, it is remarkable that the spectral index and cutoff energy lie within 1 standard deviation from that assumed by the H.E.S.S. Collaboration[18]. This implies that the assumptions made by the H.E.S.S. Collaboration on the assumed cooling break and the spectral index inferred therefrom may be described by a exponentially cutoff power law.

7.3.4 Conclusion

The spectral analyses performed in the previous sections made it possible to successfully deduce the spectral energy distribution of N 157B while simultaneously fitting the spectral parameters of 30 Dor C. For the H.E.S.S. energy range of 700 GeV to 100 TeV it was determined that the spectral shape which best represents the observed spectral data of N 157B is that of a power law. Thus, the spectral component of N 157B assumes the following form:

$$\frac{dN}{dE}(E) = (1.14 \pm 0.08) \left(\frac{E}{10^6} \right)^{-2.68 \pm 0.07} \quad (7.3.5)$$

The spectral properties determined for N 157B coincide with that of the H.E.S.S. Collaboration[18], lying within only 1.2 standard deviations of the H.E.S. value.

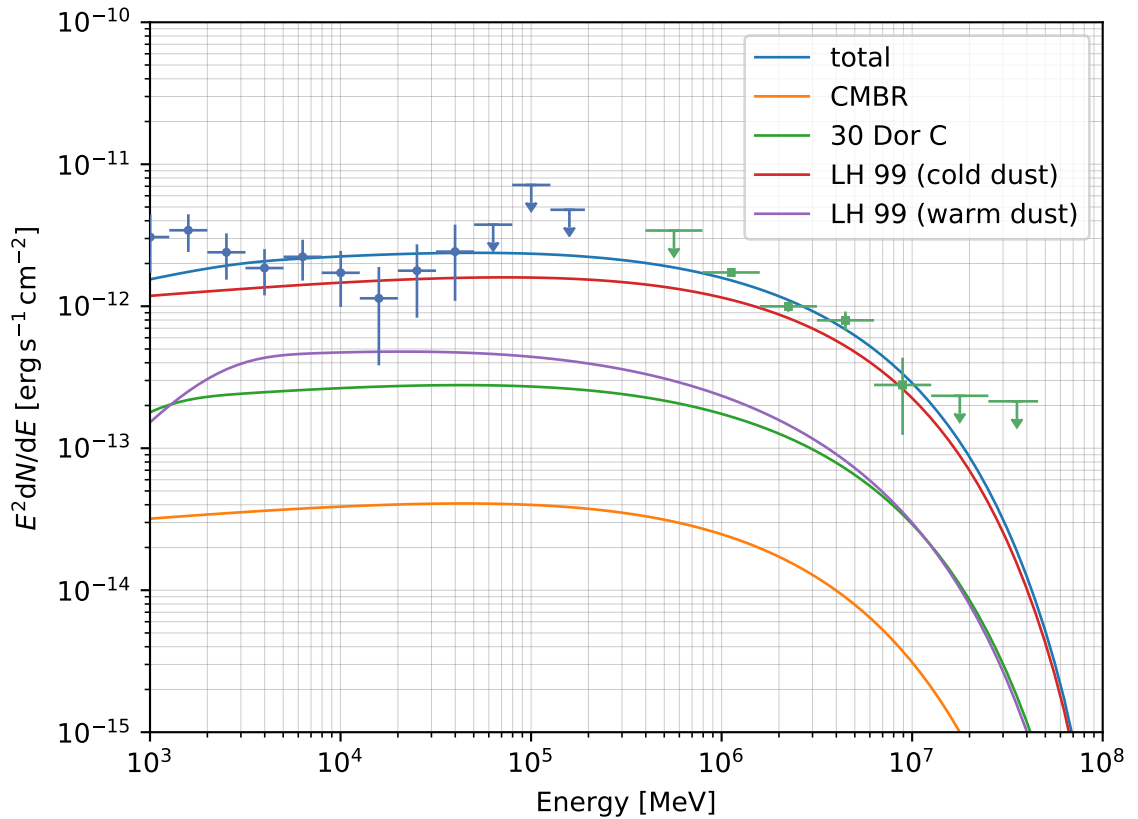


Figure 7.12: Non-Thermal Features of N 157B. Flux points of N 157B in the H.E.S.S. energy range, determined by CTools, is shown in green while the lower energy Fermi-LAT data is shown in blue. The plot shows the contribution of each radiation field to the inverse Compton emission of N 157B. The blue solid line represents the sum of contributions of all the radiation fields. The flux points accompanied by the upper limits are also present.

It follows that the spectral intensity of N 157B follows a power law throughout the energy range of 700 GeV to 100 TeV. The observed data set did not support a spectral model more complex than a power law for the H.E.S.S. energy range. Thus we were unable to detect a spectral break within the given energy range; however, a spectral break outside the H.E.S.S. energy range could exist.

The inverse Compton emission of N 157B may be attributed to the electron population scattering off different low energy photon fields associated with the cold dust and warm dust of the OB association LH 99, 30 Dor C and the cosmic microwave

background, listed in order of contribution. The electron population may be described by an exponentially cut-off power law and an inverse Compton radiative model was chosen to represent the non-thermal emission from N 157B.

A cut-off energy of $10.0_{-6.89}^{+9.61}$ TeV was determined for the combined spectrum with a spectral index of $-2.76_{-0.10}^{+0.73}$. The total energy of the relativistic electron population was found to be $1.06_{-0.54}^{+0.22} \times 10^{49}$. The large errors associated with the cut-off energy suggests that a cut-off may exist in the studied energy range, however, more TeV data is needed to confirm this. The spectral index agrees with that hypothesised by H.E.S.S.

The spectral energy distribution along with the non-thermal properties of N 157B are fitted using both H.E.S.S. and Fermi-LAT data with no assumptions being made regarding the mechanisms of the break in the spectrum. The H.E.S.S. Collaboration[18] establishes the existence of a break in the spectrum and assumes this to be a cooling break. We simply assume this break may be described by a power law with an exponential cutoff. The fact that the spectral index and cutoff energy lie within 1 standard deviation of that predicted by the H.E.S.S. Collaboration[18] implies that the assumptions made by the H.E.S.S. Collaboration on the assumed cooling break and the spectral index inferred therefrom may be described by an exponentially cutoff power law.

Like N 157B, the spectral energy distribution of 30 Dor C is described by a simple power law of Equation 7.3.6 with each spectral parameter presented within approximately 1 standard deviation of that determined by the H.E.S.S. Collaboration, with the exception of the differential flux which was found to lie within 2.22 standard deviations.

$$\frac{dN}{dE}(E) = 3.09 \pm 0.51 \left(\frac{E}{10^6} \right)^{-2.6 \pm 0.15} \quad (7.3.6)$$

It follows that while the spectral properties determined for 30 Dor C do agree with that determined by the H.E.S.S. Collaboration, a greater differential flux is

observed which is not observed for N 157B. The reason for this significant deviation is that the circular-like morphology takes into account emission from the centre of 30 Dor C as well as the outskirts. The spectral energy distribution produced by Equation (7.3.6) was found to coincide with that produced by the H.E.S.S collaboration.

Fundamentally, CTools was able to separate and fit the spectral energy distribution of two closely separated sources from which the non-thermal components of N 157B were able to be reproduced.

8. Conclusions

The goal of this project was to evaluate the CTools software package for the purpose of H.E.S.S. data analysis. The problem of determining the morphology and the spectrum of multiple sources with small off-sets and varying spectral shapes was addressed. The current approach involves fitting the morphology and spectrum of each source under consideration separately and ignoring any spillovers. While robust, this approach is valid under the assumption that the sources are separated by more than 1° or that they bear similar spectral shapes, which is not always the case.

CTools was proposed as a solution as it is able to simultaneously fit the spectra and morphologies of multiple sources, with varying spectral and morphological properties, while accounting for spillovers. In order to determine the validity of CTools as a means of H.E.S.S. data analysis, we evaluated the CTools analysis framework on simulated CTA data and applied the framework to existing H.E.S.S data of the Large Magellanic Cloud (LMC).

The application domain of the software includes simulated data of the Crab Nebula in conjunction with H.E.S.S. data of 30 Dor C and N 157B within the LMC. Results were considered significant if a significance of 5.3σ or greater was achieved in comparisons with null models.

Initially the sensitivity of CTools to detect a cutoff energy of a single gamma ray emitter, that being the Crab Nebula, for a simulated CTA data set was evaluated. By means of likelihood and significance comparisons, it was found that software was

able to position the cutoff energy of a gamma ray source within the energy range of 0.14 TeV to 12 TeV. Thus, the lower and upper limits for which a deviation from a power-law spectrum may be detected by CTools for a CTA data set were successfully determined.

Thereafter, the degree of resolution of the CTools software was explored by analysing two closely separated gamma-ray emitting sources, the Crab Nebula and a 90% dimmer pseudo source, for a simulated CTA data set. It was possible to spatially distinguish two CTA sources up to an offset of 0.05° while simultaneously fitting the spectra of the two sources in the case where contamination from the neighbouring source is a factor. Therefore, the minimum offset angle for which two gamma-ray sources may be resolved by CTools for a CTA data set was successfully determined.

After successfully applying CTools to simulated CTA data the next logical step was to analyse CTools software on real data, that is H.E.S.S. data, by fitting the morphology and spectrum of gamma-ray emitters in the LMC, namely N 157B and 30 Dor C. These emitters are separated by a mere 0.15° and differ in flux by a factor of 10.

The morphological aspect of the analysis included simultaneously fitting various morphologies to 30 Dor C and the position of N 157B. We concluded that 30 Dor C assumes a radial disk-like morphology which coincides with its superbubble-like nature. A right ascension and declination of $84.0^\circ \pm 0.02^\circ$ and $-69.17^\circ \pm 0.01^\circ$, respectively, and a radius of $0.08^\circ \pm 0.009^\circ$ was determined for 30 Dor C. N 157B was assumed to be a point source and found to have a right ascension of $84.45^\circ \pm 0.01^\circ$ and a declination of $-69.16^\circ \pm 0.001^\circ$.

These results agrees with those of the H.E.S.S. Collaboration and with data in the X-ray regime which is probable cause to assume that CTools was successful in determining the morphology of 30 Dor C while fitting the position of N 157B. That

is, the software was able to successfully distinguish two sources with an offset of 0.15° where source contamination is a factor and one source is outshined by its companion.

The spectral aspect of the analysis involved the simultaneous fitting of the spectra of various spectral shapes to N 157B and fitting the spectral parameters of 30 Dor C. The best fit parameters of 30 Dor C were found to be a value of -2.57 ± 0.15 for the spectral index and $3.09 \times 10^{-18} \text{ph.cm}^{-2}.\text{s}^{-1}.\text{MeV}^{-1}$ for the differential flux. While the differential flux is higher than anticipated, these parameters are able to produce a spectral energy distribution which aligns with that of the H.E.S.S. Collaboration[18].

No deviation in the spectral energy distribution was determined for N 157B; thus, it was found that a simple power-law with a spectral index of -2.67 ± 0.07 and a differential flux of $1.14 \pm 0.08 \times 10^{-19} \text{ph.cm}^{-2}.\text{s}^{-1}.\text{MeV}^{-1}$ was the most appropriate in representing its spectrum. Since no spectral break or curvature was found in the H.E.S.S. energy range of 700 GeV to 100 TeV, a more in-depth study attempted to produce a model explaining the non-thermal features of N 157B over a greater energy range while searching for a cutoff energy.

A lower energy cut-off may be tested for by combining lower energy gamma ray Fermi-LAT data of N 157B with that of CTools. It was concluded that the inverse Compton emission of N 157B may be attributed to the electron population scattering off the photon fields associated with the cold dust and warm dust of the OB association LH 99, 30 Dor C and the cosmic microwave background, listed in order of contribution. The electron population may be modeled by an exponentially cut off power law and the non-thermal emissions may be described by an inverse Compton radiative model.

Upon fitting the multi-wavelength spectrum, we found a low energy cut-off of $10.0_{-6.89}^{+9.61}$ TeV. The large associated error indicates that more TeV observations are needed. A spectral index of $-2.76_{-0.10}^{+0.73}$ was fitted which is in complete agreement

with that assumed by the H.E.S.S. Collaboration. The total energy of the electron population was found to be $1.06_{-0.54}^{+0.22} \times 10^{49}$ erg.

As previously established, this is the first time that the spectral energy distribution along with the non-thermal properties of N157B are fitted using both H.E.S.S. and Fermi-LAT data. There were no assumptions made in regards to the mechanisms of the break present in the spectrum. It was only assumed that the already established break could be described by a power law with a cutoff. It is remarkable that the spectral index and the cutoff energy may be fitted within 1 standard deviation from that assumed by the H.E.S.S. Collaboration[18].

It follows that the assumptions made by the H.E.S.S. Collaboration on the assumed cooling break and the spectral index inferred therefrom are quite plausible. Ultimately, CTools was able to separate and fit the spectral energy distribution of two closely separated sources from which the non-thermal components of N 157B were able to be reproduced.

Thus the principal conclusion follows that the CTools software package is successful and effective in analysing gamma-ray emitters in the TeV regime where these emitters are closely separated, with an offset of less than 1° , below which emitters with vastly different spectral shapes may not be simultaneously compared and studied. Not only is CTools able to simultaneously fit the spectra of two emitters of varying spectral shapes at this offset but is also able to spatially separate such gamma-ray emitters while taking any spillovers into account.

Since CTools was determined to be a viable means of TeV gamma-ray analysis, as the application of CTools to historical H.E.S.S. data was a success, the next intuitive phase would be to use the software to analyse currently under-studied TeV gamma-ray sources. This attempt would entail investigating if the application of CTools to these under-studied sources may reveal any new features or insights of the sources at hand.

Bibliography

- [1] Jamie Holder. TeV gamma-ray astronomy: A summary. *Astroparticle Physics*, 39:61–75, 2012.
- [2] Klaus Pinkau. History of gamma-ray telescopes and astronomy. *Experimental Astronomy*, 25(1-3):157–171, 2009.
- [3] Bernard Degrange and Gérard Fontaine. Introduction to high-energy gamma-ray astronomy. *Comptes Rendus Physique*, 16(6-7):587–599, 2015.
- [4] PA Cerenkov. Visible Radiation Produced by Electrons Moving in a Medium with Velocities Exceeding that of Light. *Phys. Rev.*, 52:378, 1937.
- [5] Alan A Watson. The discovery of Cherenkov radiation and its use in the detection of extensive air showers. *Nuclear Physics B-Proceedings Supplements*, 212:13–19, 2011.
- [6] JV Jelley and W Galbraith. Light pulses from the night sky and Cherenkov radiation Part II. *Journal of Atmospheric and Terrestrial Physics*, 6(1-6):304–312, 1955.
- [7] P. Morrison. On gamma-ray astronomy. *Il Nuovo Cimento (1955-1965)*, 7(6):858–865, Mar 1958.
- [8] G Cocconi. An air shower telescope and the detection of 10^{12} eV photon sources. In *International Cosmic Ray Conference*, volume 2, page 309, 1960.
- [9] Trevor C Weekes, MF Cawley, DJ Fegan, KG Gibbs, AM Hillas, PW Kowk, RC Lamb, DA Lewis, D Macomb, NA Porter, et al. Observation of TeV gamma

- rays from the Crab nebula using the atmospheric Cerenkov imaging technique. *The Astrophysical Journal*, 342:379–395, 1989.
- [10] Michael Punch, Carl W Akerlof, MF Cawley, M Chantell, DJ Fegan, S Fennell, JA Gaidos, J Hagan, AM Hillas, Y Jiang, et al. Detection of TeV photons from the active galaxy Markarian 421. *Nature*, 358(6386):477, 1992.
- [11] F Aharonian, A Akhperjanian, M Beilicke, K Bernlöhr, H-G Börst, H Bojahr, O Bolz, T Coarasa, JL Contreras, J Cortina, et al. Is the giant radio galaxy M87 a TeV gamma-ray emitter? *Astronomy & Astrophysics*, 403(1):L1–L5, 2003.
- [12] A Neronov and Felix A Aharonian. Production of TeV gamma radiation in the vicinity of the supermassive black hole in the giant radio galaxy M87. *The Astrophysical Journal*, 671(1):85, 2007.
- [13] H.E.S.S. Collaboration and others. The exceptionally powerful TeV γ -ray emitters in the Large Magellanic Cloud. *Science*, 347(6220):406–412, 2015.
- [14] Markus Ackermann, A Albert, WB Atwood, Luca Baldini, J Ballet, Guido Barbiellini, D Bastieri, R Bellazzini, E Bissaldi, ED Bloom, et al. Deep view of the Large Magellanic Cloud with six years of Fermi-Lat observations. *Astronomy & Astrophysics*, 586:A71, 2016.
- [15] J Knödseder, M Mayer, C Deil, J-B Cayrou, E Owen, N Kelley-Hoskins, C-C Lu, R Buehler, F Forest, T Louge, et al. Gammalib and ctools-a software framework for the analysis of astronomical gamma-ray data. *Astronomy & Astrophysics*, 593:A1, 2016.
- [16] L Mohrmann, K Nakashima, A Specovius, D Tiziani, S Funk, C van Eldik, and S Ohm. Towards a 3D likelihood analysis in very-high-energy γ -ray astronomy: the case of H.E.S.S. In *ICRC*, volume 36, page 747, 2019.
- [17] J Knödseder, L Tibaldo, D Tiziani, A Specovius, J Cardenzana, M Mayer, N Kelley-Hoskins, L Di Venere, S Bonneyfof, A Ziegler, et al. Analysis of the

- H.E.S.S. public data release with CTools. *Astronomy & Astrophysics*, 632:A102, 2019.
- [18] A Abramowski, Fabio Acero, F Aharonian, AG Akhperjanian, G Anton, S Balenderan, A Balzer, A Barnacka, Y Becherini, J Becker, et al. Discovery of gamma-ray emission from the extragalactic pulsar wind nebula N 157B with H.E.S.S. *Astronomy & Astrophysics*, 545:L2, 2012.
- [19] Patrick Slane. Pulsar wind nebulae. *arXiv preprint arXiv:1703.09311*, 2017.
- [20] E. G. Berezhko and H. J. Völk. Hadronic versus leptonic origin of the gamma-ray emission from supernova remnant RX-J1713.7-3946. *A&A*, 492(3):695–701, 2008.
- [21] FA Aharonian, AG Akhperjanian, JA Barrio, K Bernlöhr, H Bojahr, I Calle, JL Contreras, J Cortina, S Denninghoff, V Fonseca, et al. The energy spectrum of TeV gamma rays from the Crab Nebula as measured by the HEGRA system of imaging air Cerenkov telescopes. *The Astrophysical Journal*, 539(1):317, 2000.
- [22] Felix Aharonian, AG Akhperjanian, AR Bazer-Bachi, M Beilicke, Wystan Benbow, David Berge, K Bernlöhr, C Boisson, Oliver Bolz, V Borrel, et al. Observations of the Crab nebula with H.E.S.S. *Astronomy & Astrophysics*, 457(3):899–915, 2006.
- [23] Fermi LAT Collaboration and others. An extremely bright gamma-ray pulsar in the Large Magellanic Cloud. *Science*, 350(6262):801–805, 2015.
- [24] EJ Murphy, TA Porter, IV Moskalenko, G Helou, and AW Strong. Characterizing cosmic-ray propagation in massive star-forming regions: The case of 30 Doradus and the Large Magellanic Cloud. *The Astrophysical Journal*, 750(2):126, 2012.
- [25] Hiroya Yamaguchi, Aya Bamba, and Katsuji Koyama. Suzaku Observation of 30 Dor C: A Supernova Remnant with the Largest Non-Thermal Shell. *Publications of the Astronomical Society of Japan*, 61(sp1):S175–S181, 2009.

- [26] You-Hua Chu. Bubbles and superbubbles: Observations and theory. *Proceedings of the International Astronomical Union*, 3(S250):341–354, 2007.
- [27] Cathie Clarke, Bob Carswell, and RF Carswell. *Principles of astrophysical fluid dynamics*. Cambridge University Press, 2007.
- [28] Stephen P Reynolds. Models of synchrotron X-rays from shell supernova remnants. *The Astrophysical Journal*, 493(1):375, 1998.
- [29] Knox S Long, David J Helfand, and David Andrew Grabelsky. A soft X-ray study of the Large Magellanic Cloud. *The Astrophysical Journal*, 248:925–944, 1981.
- [30] K Dennerl, F Haberl, B Aschenbach, UG Briel, M Balasini, H Bräuninger, W Burkert, R Hartmann, G Hartner, Gunther Hasinger, et al. The first broadband X-ray images and spectra of the 30 Doradus region in the LMC. *Astronomy & Astrophysics*, 365(1):L202–L207, 2001.
- [31] AE Le Marne and BY Mills. High resolution observations of the 30 Doradus Nebula at 408 MHz. *Monthly Notices of the Royal Astronomical Society*, 139(4):461–469, 1968.
- [32] BY Mills, AJ Turtle, AG Little, and JM Durdin. A new look at radio supernova remnants. *Australian Journal of Physics*, 37(3):321–358, 1984.
- [33] DS Mathewson, VL Ford, IR Tuohy, BY Mills, AJ Turtle, and DJ Helfand. Supernova remnants in the Magellanic Clouds. III. *The Astrophysical Journal Supplement Series*, 58:197–200, 1985.
- [34] Bryan M Gaensler and Patrick O Slane. The evolution and structure of pulsar wind nebulae. *Annu. Rev. Astron. Astrophys.*, 44:17–47, 2006.
- [35] Q Daniel Wang and Eric V Gotthelf. ROSAT and ASCA observations of the Crab-like supernova remnant N 157B in the Large Magellanic Cloud. *The Astrophysical Journal*, 494(2):623, 1998.
- [36] Walter Heitler. *The Quantum Theory of Radiation*. 1984.

- [37] James Matthews. A Heitler Model of Extensive Air Showers. *Astroparticle Physics*, 22(5-6):387–397, 2005.
- [38] N.M.Nagy J.Konya. Nuclear and Radiochemistry. pages 83–127, 2012.
- [39] M.F. L’Annunziata. Handbook of Radioactivity Analysis. 3:935–1019, 2012.
- [40] A.M. Hillas. Differences Between Gamma-ray Showers and Hadronic Showers. *Space Science Reviews*, 75(1-2):17–30, 1996.
- [41] Trevor C Weekes. The atmospheric Cherenkov technique in very high energy gamma-ray astronomy. *Space Science Reviews*, 75(1-2):1–15, 1996.
- [42] K Bernlöhner, O Carrol, R Cornils, S Elfahem, P Espigat, S Gillessen, G Heinzelmann, G Hermann, W Hofmann, D Horns, et al. The optical system of the H.E.S.S. imaging atmospheric Cherenkov telescopes. Part I: layout and components of the system. *Astroparticle Physics*, 20(2):111–128, 2003.
- [43] C Venter. The status of H.E.S.S. and CTA, and their role in a multiwavelength context. 2012.
- [44] BK Lubsandorshiev. Multi-TeV Gamma-Ray Astronomy. 2016.
- [45] Benbow, Wytan and H.E.S.S. Collaboration. The status and performance of H.E.S.S. In *AIP Conference Proceedings*, volume 745, pages 611–616. American Institute of Physics, 2005.
- [46] M Actis, G Agnetta, Felix Aharonian, A Akhperjanian, J Aleksić, E Aliu, D Allan, I Allekotte, F Antico, LA Antonelli, et al. Design concepts for the Cherenkov Telescope Array CTA: an advanced facility for ground-based high-energy gamma-ray astronomy. *Experimental Astronomy*, 32(3):193–316, 2011.
- [47] Hamish Silverwood, Christoph Weniger, Pat Scott, and Gianfranco Bertone. A realistic assessment of the CTA sensitivity to dark matter annihilation. *Journal of Cosmology and Astroparticle Physics*, 2015(03):055, 2015.
- [48] Jianqing Fan, Chunming Zhang, Jian Zhang, et al. Generalized likelihood ratio statistics and Wilks phenomenon. *The Annals of statistics*, 29(1):153–193, 2001.

- [49] Carlo Romoli, Andrew M Taylor, and Felix Aharonian. Cut-off characterisation of energy spectra of bright Fermi sources: Current instrument limits and future possibilities. *Astroparticle Physics*, 88:38–45, 2017.
- [50] Attila Abramowski, F Aharonian, F Ait Benkhali, AG Akhperjanian, EO Angüner, M Backes, S Balenderan, A Balzer, A Barnacka, Y Becherini, et al. H.E.S.S. detection of TeV emission from the interaction region between the supernova remnant G349.7+0.2 and a molecular cloud. *Astronomy & Astrophysics*, 574:A100, 2015.
- [51] Mathieu De Naurois and Loic Rolland. A high performance likelihood reconstruction of γ -rays for imaging atmospheric Cherenkov telescopes. *Astroparticle Physics*, 32(5):231–252, 2009.
- [52] V. Zabalza. Naima: a Python package for inference of relativistic particle energy distributions from observed nonthermal spectra. *Proc. of International Cosmic Ray Conference 2015*, page 922, 2015.

Appendix A

A.1 Model Definition File

```
<?xml version='1.0' encoding='UTF-8' standalone='no'?>
<source_library title='source library'>
<source name='N157B' type='PointSource' tscal='1'>
<spectrum type='PowerLaw'>
<parameter name='Prefactor' value='1' error='0' scale='1e-18' min='1e-09' max='1000000' free='1' />
<parameter name='Index' value='2.5' error='0' scale='-1' min='0' max='5' free='1' />
<parameter name='PivotEnergy' value='1' scale='1000000' min='0.0001' max='10000' free='0' />
</spectrum>
<spatialModel type='SkyDirFunction'>
<parameter name='RA' value='84.4448167' error='0' scale='1' min='83' max='86' free='1' />
<parameter name='DEC' value='-69.172667' error='0' scale='1' min='-71' max='-68' free='1' />
</spatialModel>
</source>
<source name='30DorC' type='PointSource' tscal='1'>
<spectrum type='PowerLaw'>
<parameter name='Prefactor' value='1' error='0' scale='1e-19' min='1e-09' max='1000000' free='1' />
<parameter name='Index' value='2.5' error='0' scale='-1' min='0' max='5' free='1' />
<parameter name='PivotEnergy' value='1' scale='1000000' min='0.0001' max='10000' free='0' />
</spectrum>
<spatialModel type='SkyDirFunction'>
<parameter name='RA' value='83.8807' scale='1' min='-360' max='360' free='1' />
<parameter name='DEC' value='-69.2074' scale='1' min='-360' max='360' free='1' />
</spatialModel>
</source>
<source name='bkg_23716' type='CTAIrfBackground' instrument='HESS' id='23716' tscal='0'>
<spectrum type='Constant'>
<parameter name='Normalization' value='2.0431225' error='0' scale='1' min='0.020431' max='204.312252' free='1' />
</spectrum>
</source>
<source name='bkg_23736' type='CTAIrfBackground' instrument='HESS' id='23736' tscal='0'>
...
```

Table A.1: General Format Of A Model Definition File

Table [A.1](#) contains three source models, namely a background model as well as source models for N 157B and 30 DorC. It can be seen that the models **consists** two components, namely a spatial and spectral model component. A temporal model component may also be included which will illustrate the dependence of the brightness or light intensity of a gamma-ray emitter on time. For the purpose of the project, a temporal model component was not necessary and, therefore, omitted. The 'error' term for all parameters is currently defined as zero. After fitting the model to a data set this term will be adjusted to the uncertainty associated with the respective parameter. Parameters which are to be fitted will have the attribute 'free=1' while those which are required to remain fixed will have the attribute 'free=0'.

A.2 Observation Definition File

The observation definition file consists an observation list consisting of several gamma-ray observations defined by a specific observation ID accompanied by information regarding the the location of the event lists as well as IRF details. The observation definition file presented in table [A.2](#) **consists** the gamma-ray observations of the LMC by H.E.S.S.

```

<?xml version="1.0" encoding="UTF-8" standalone="no"?>
<observation_list title="observation list">
<observation name="SN 1987A" id="23716" instrument="HESS">
<parameter name="EventList" file="/HddData/hess/data/fts/pa/release-1.0/Model_Deconvoluted_Prod26/Mpp_HiRes/run023716/events_023716.fits.gz[EVENTS]" />
<parameter name="EffectiveArea" file="/HddData/hess/data/fts/pa/release-1.0/Model_Deconvoluted_Prod26/Mpp_HiRes/run023716/aeff_023716.fits.gz[EFFECTIVE AREA]" />
<parameter name="PointSpreadFunction" file="/HddData/hess/data/fts/pa/release-1.0/Model_Deconvoluted_Prod26/Mpp_HiRes/run023716/psf_king_023716.fits.gz[POINT SPREAD FUNCTION]" />
<parameter name="EnergyDispersion" file="/HddData/hess/data/fts/pa/release-1.0/Model_Deconvoluted_Prod26/Mpp_HiRes/run023716/edisp_023716.fits.gz[ENERGY DISPERSION]" />
<parameter name="Background" file="/HddData/hess/data/fts/pa/release-1.0/Model_Deconvoluted_Prod26/Mpp_HiRes/background/bgnmodel_alt6_az1.fits.gz[BACKGROUND]" />
</observation>
<observation name="SN 1987A" id="23736" instrument="HESS">
<parameter name="EventList" file="/HddData/hess/data/fts/pa/release-1.0/Model_Deconvoluted_Prod26/Mpp_HiRes/run023736/events_023736.fits.gz[EVENTS]" />
<parameter name="EffectiveArea" file="/HddData/hess/data/fts/pa/release-1.0/Model_Deconvoluted_Prod26/Mpp_HiRes/run023736/aeff_023736.fits.gz[EFFECTIVE AREA]" />
<parameter name="PointSpreadFunction" file="/HddData/hess/data/fts/pa/release-1.0/Model_Deconvoluted_Prod26/Mpp_HiRes/run023736/psf_king_023736.fits.gz[POINT SPREAD FUNCTION]" />
<parameter name="EnergyDispersion" file="/HddData/hess/data/fts/pa/release-1.0/Model_Deconvoluted_Prod26/Mpp_HiRes/run023736/edisp_023736.fits.gz[ENERGY DISPERSION]" />
<parameter name="Background" file="/HddData/hess/data/fts/pa/release-1.0/Model_Deconvoluted_Prod26/Mpp_HiRes/background/bgnmodel_alt6_az1.fits.gz[BACKGROUND]" />
</observation>
<observation name="SN 1987A" id="23737" instrument="HESS">
..

```

Table A.2: General Format of an Observation Definition File

A.3 Abbreviations Used

- **IACT**: Imaging Atmospheric Cherenkov Telescope
- **H.E.S.S.**: High Energy Stereoscopic System
- **CTA**: Cherenkov Telescope Array
- **PSF**: Point Spread Function
- **IRF**: Instrument Response Function
- **LMC**: Large Magellanic Cloud
- **MAGIC**: Major Atmospheric Gamma Imaging Cherenkov Telescopes
- **VERITAS**: Very Energetic Radiation Imaging Telescope Array System
- **COMPTEL**: Compton Telescope
- **Fermi-LAT**: Fermi Large Area Telescope
- **HEGRA**: High Energy Gamma Ray Astronomy
- **SNR**: Super Nova Remnant
- **PWN(e)**: Pulsar Wind Nebula(e)
- **FITS**: Flexible Image Transport System